Waterborne polyester/CD@TiO_2 nanocomposite for multi-faceted applications

Highlights

This chapter deals with the fabrication of carbon dot (CD)@TiO_2-based waterborne hyperbranched polyester (WHPE) nanocomposite to achieve a combined special attributes of anti-icing, anti-fogging, anti-reflecting, self-cleaning, etc. properties in a single material. The chapter is divided into two sub-chapters, where first sub-chapter describes the synthesis, characterization and evaluation of photocatalytic activity of CD@TiO_2 nanohybrid. Second chapter deals with the fabrication, characterization and property evaluation of WHPE/(CD)@TiO_2 nanocomposites. Significant enhancements in tensile strength, toughness, Young's modulus, gloss and thermal stability were observed for the thermosets by formation of nanocomposite. They also exhibited wavelength dependent both down- and up-conversion photoluminescence (PL) properties. Further, the nanocomposite can be used as a photocatalyst for reduction of 4-nitrophenol (4-NP) to aminophenol under normal sunlight. More interestingly, it can also be used for efficient separation of crude oil and water from their mixture. Thus, these environmentally benign polymeric materials could be used for different advanced applications.

Parts of this chapter are published in

1. **Hazarika, D.** and Karak, N. Photocatalytic degradation of organic contaminants under solar light using carbon dot/titanium dioxide nanohybrid, obtained through a facile approach. *Applied Surface Science*, 376:276-285, 2016.
2. **Hazarika, D.** and Karak, N. Unprecedented influence of carbon dot@TiO_2 nanohybrid on multi-faceted attributes of waterborne hyperbranched polyester nanocomposite. *ACS Omega*, 3(2):1757-1769, 2018.
3. **Hazarika, D.**, Saikia, D., Gupta, K., Mandal, M., and Karak, N. Photoluminescence, self cleaning and photocatalytic behavior of waterborne hyperbranched polyester/carbon dot@TiO_2nanocomposite. *Chemistry Select*, 3(22):6126-6135, 2018.

6A. Synthesis of CD@TiO_2 nanohybrid by hydrothermal method

6A.1. Introduction

Photocatalysis by semiconductor is gaining significant interest to all as a green technology and an energy sustainable solution. This is because of the fact that it can be widely used for removal of different hazardous organic pollutants and thereby purifying the environment [1-3]. TiO_2 is one of the promising members as a semiconductor which is extensively used in the field of photocatalysis owing to its special attributes like abundances, nontoxic nature, physico-chemical stability, cost-effectiveness, etc. It is a highly efficient photocatalyst under excitation as photogenerated electrons and holes, which are strong oxidising and reducing agents [3, 4]. However, UV light responsivity of TiO_2 due to its larger band gap (3.2 eV) and rapid recombination of photogenerated electrons and hole limits its use in many practical applications [3-5]. Therefore, it has been challenging to found realistic design criteria and preparative protocols for visible-light active TiO_2 system which facilitate more efficient utilization of solar spectrum. Many studies have found that CD can enhance photocatalytic activity under visible light irradiation. CD/rutile TiO_2 was developed by Zhang *et al.* [6] through a multi-step processes which comprises of preparation of CD and TiO_2 array, adsorption of CD on the surface of TiO_2 array followed by annealing. Fabrication CD/TiO_2 nanosheet composite by the mixture of prepared CD and TiO_2 nanosheet was also reported [7]. Nitrogen-doped CD/rutile TiO_2 hierarchical microspheres were synthesized by Huang *et al.* [8] through hydrothermal treatment of $TiCl_3$ in the presence of CD. However, all these reported methods are time-consuming, tedious and unfavourable for large scale production. In addition, most of the CD-loaded nanohybrids are prepared by only physical blending without any chemical coupling, which may lead to poor performance [9-13]. Thus, in this study, we have attempted to synthesize CD@TiO_2 nanohybrid using the same carbon precursors of CD as described in **Chapter 4** along with titanium butoxide by a one pot single step facile and green technique (both *in-situ* and *ex-situ* method). The resultant nanohybrids integrated the fluorescence properties of CD with the mechanical, magnetic and optical properties of the metal oxides and act as efficient photocatalysts [9, 14-17]. The self-cleaning properties of TiO_2 originate from the photocatalytic oxidative decomposition of organic contaminants. Again, among different types of organic pollutants, phenol and benzene are highly toxic and carcinogenic compounds, produced from different chemical industries [11]. Therefore, both *in-situ*

(CD@TiO_2) and *ex-situ* (CD/TiO_2) synthesized nanohybrids were utilized for photocatalytic degradations of these pollutants. Further, amongst different hazardous anthropogenic organic chemicals, pesticides are the most common non-degradable anthropogenic chemical contaminants both in water and soil [18]. Therefore, synthesized nanohybrids were also tested for degradation of a representative paraxon pesticide.

Authors, therefore, wish to report a facile one-step green synthetic protocol for synthesis of highly fluorescent CD@TiO_2 nanohybrid from bio-based carbon precursors. This nanohybrid was used as an efficient photocatalyst for degradation of organic pollutants like benzene and phenol, and a representative pesticide under normal sunlight. The bare CD, TiO_2 and CD/TiO_2 nanomaterials were also prepared to judge the superiority of *in-situ* synthesized CD@TiO_2 nanohybrid for the same purpose.

6A.2. Experimental

6A.2.1. Materials

The materials and precursors used for preparation of CD were the same as described in **Chapter 4**. Titanium butoxide used for preparation of bare TiO_2 and the nanohybrid, was purchased from Sigma Aldrich, Germany. Phenol and benzene were obtained from Merck, India and used in this study to check the photocatalytic ability of the nanomaterials. Ethyl paraoxon pesticide used in photocatalytic reaction was obtained from Sigma Aldrich, Germany. It is one of the most common non-degradable anthropogenic chemical contaminants both in water and soil, and used in industry as well as in agriculture.

6A.2.2. Characterization

FTIR, SEM and TGA analyses were performed by using the same instruments under the same conditions as described in **sub-Chapter 2A, sub-section 2A.2.2**. UV and PL analyses were carried out using the same instruments as mentioned in **Chapter 4, section 4.2**. The morphology and SAED pattern of the nanomaterials were analyzed by the same HRTEM as mentioned in **Chapter 3, section 3.2.**

6A.2.3. Synthesis of bare TiO_2

Bare TiO_2 nanoparticles were synthesized by a single step hydrothermal process. Firstly, 15 mL of concentrated HCl was mixed with 5 mL of distilled water and 10 mL cow urine

and the mixture was stirred for 10 min. Then, 0.8 mL of titanium butoxide was added dropwise to the above mixture. After vigorously stirring for another 10 min, the solution was transferred to a 50 mL Teflon lined stainless steel autoclave which was kept in a muffle furnace at 150 °C for 8 h. The autoclave was cooled down to room temperature. Then the solution was centrifuged at 5000 rpm for 15 min and dried at 50 °C for 7-8 h to obtain the solid residue. This solid product was calcined at 300 °C for 2 h in a muffle furnace.

6A.2.4. Synthesis of nanohybrids of CD and TiO_2

CD and TiO_2 nanohybrids were synthesized by both *in-situ* and *ex-situ* techniques. In an *in-situ* technique, at first equal amount (0.668 g) of citric acid and glycerol was mixed with 5 mL water, 10 mL cow urine and 15 mL concentrated HCl and the mixture was continuously stirred for 10 min. To the above mixture, 1.6 mL titanium butoxide was added dropwise and stirred for another 10 min. Then the above mixture was transferred to a 50 mL Teflon lined stainless steel autoclave which was placed in a muffle furnace and heated at 150 °C for 8 h. The autoclave was cooled to room temperature and the suspension obtained after the reaction was centrifuged at 5000 rpm for 15 min and dried at 50 °C for 5-7 h in an oven for further use. The obtained nanohybrid was coded as CD@TiO_2.

In *ex-situ* technique, 0.25 g CD was mixed with 5 mL water, 10 mL cow urine and 15 mL concentrated HCl by continuous stirring for 5 min. Then, 0.8 mL titanium butoxide was added dropwise to the above mixture and stirred the mixture for another 10-15 min. In the same way, as above the mixture was taken in an autoclave and heated at 150 °C for 8 h inside a muffle furnace. The autoclave was cooled down at room temperature. The obtained suspension was centrifuged like CD@TiO_2 and obtained product was dried at 50 °C for 5-7 h. This nanohybrid was coded as CD/TiO_2.

6A.2.5. Photocatalytic activity

Ethyl paraoxon organophosphate pesticide and organic pollutants like phenol and benzene were chosen for the determination of photocatalytic degradation activity of the CD@TiO_2 nanohybrid. In a typical procedure for the study of photodegradation of pesticide, required amount of CD@TiO_2 (1g/L) was taken in 50 mL aqueous solution of pesticide (10 ppm) and the solution was stirred under normal solar light (60000-80000 lux) at room temperature. The experiment was also done for bare TiO_2, CD and CD/TiO_2

for comparison purpose. The change in concentration of the pesticide was monitored by determining UV absorbance intensity at wavelength of 300 nm for the specified time intervals [18]. The activity of the catalyst was calculated from the rate of change of concentration of pesticide. The aqueous dispersions of phenol and benzene were prepared by taking the required amount of CD@TiO_2 (1g/L) in a 200 mL aqueous dispersion of phenol (50 mg/L) and benzene (100 mg/L) separately, for the study of photocatalytic degradation of them. The dispersions were stirred at room temperature under normal sunlight. After the specified time interval, 10 mL solution was drawn and centrifuged at 3000 rpm for 5 min and subsequently filtered to separate TiO_2 nanomaterials. The concentrations of phenol and benzene in the filtrate were measured quantitatively using UV absorbance intensity at wavelength of 270 nm and 250 nm respectively [10, 19, 20]. The same experiment was done for CD, bare TiO_2 and CD/TiO_2 for comparison purpose. Degradation of benzene, phenol and pesticide was calculated by using the same equation as mentioned in **Chapter 4** [10, 18].

6A.3.Results and discussion

6A.3.1. Synthesis

In order to improve the photocatalytic activity of TiO_2, researchers devoted a lot of efforts and found that the hybrid of TiO_2 with other nanomaterials efficiently broadened the range of optical response of the hybrid catalyst [10, 11, 18]. Here, nanohybrid of TiO_2 with CD was synthesized by a one pot single step hydrothermal protocol using the bio-based renewable carbon resources and titanium butoxide (*in-situ*, CD@TiO_2) to achieve efficient photocatalytic activity under the normal sunlight (**Scheme 6A.1**). The hydrothermal decomposition of titanium butoxide in the presence of CD (*ex-situ*, CD/TiO_2) was also resulted a nanohybrid. Here, HCl may help in hydrolysis of carbohydrate along with citric acid present in the system. In these nanohybrids, CD delays the recombination process of electron and hole in TiO_2. One of the greatest advantages of this approach is doping of nitrogen in the synthesized nanohybrid and CD without using any additional agent or reaction step. Nitrogen was coming from cow urine as it contains different nitrogen containing components like urea, uric acid, ammonia, etc. In CD@TiO_2 nanohybrid, TiO_2 is in anatase form, whereas in CD/TiO_2 nanohybrid, TiO_2 is present in both anatase and rutile forms (as discussed latter). The aqueous solutions of CD@TiO_2 were brown in color under daylight but showed blue and green

fluorescence under UV light at different wavelengths (**Scheme 6A.1**).

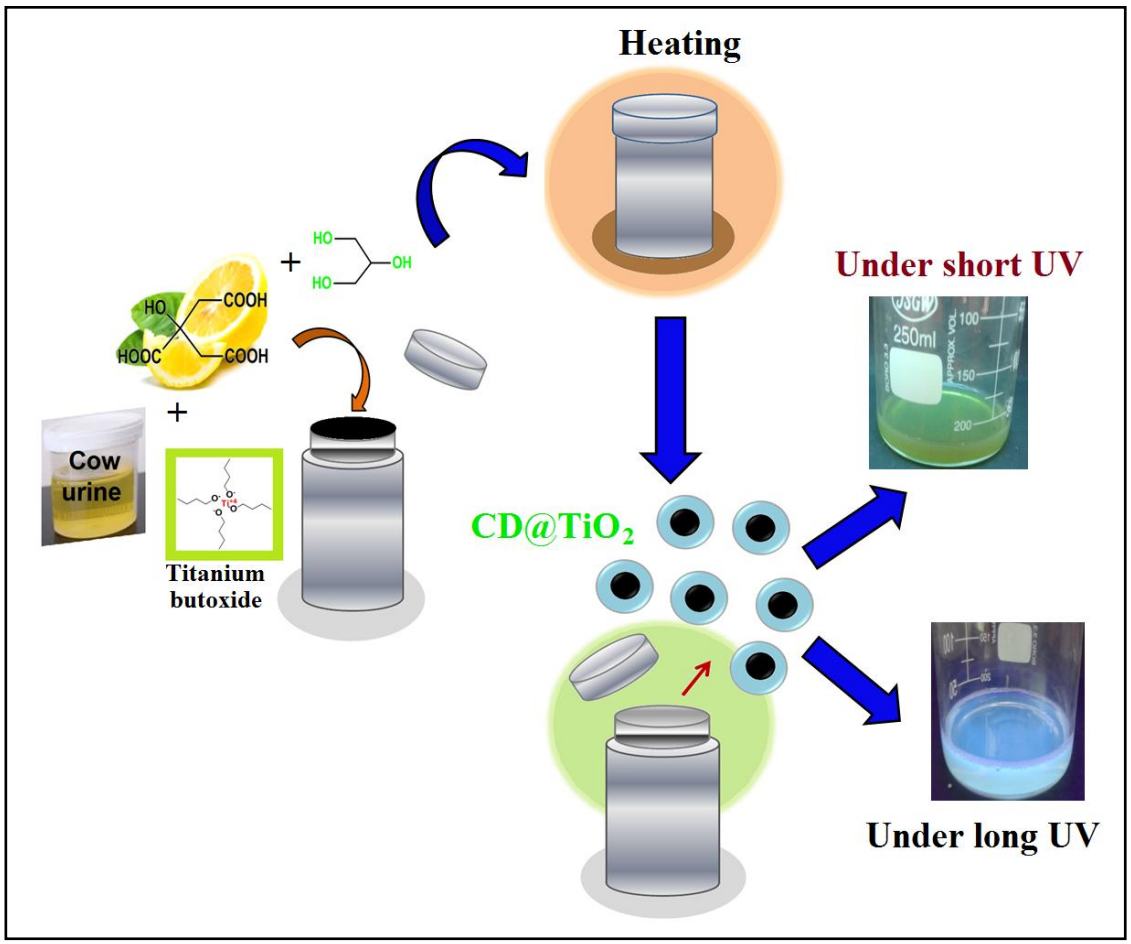

Scheme 6A.1: Synthesis of CD@TiO_2 nanohybrid and its emission of different colors under UV light

6A.3.2. Characterization

TEM images (**Figure 6A.1a-f**) of CD@TiO_2 nanohybrid demonstrated that TiO_2 nanoparticles are well-dispersed on the surface of CD. Further, the merged fringes confirmed the modification of CD on the surface of TiO_2 nanoparticles. **Figure 6A.1d-f** shows that the crystal lattice fringes with a d-spacing of 0.35 nm corresponding to the (101) plane of anatase TiO_2 which suggests that TiO_2 nanoparticles possess a high degree of crystallinity and a well-ordered structure [3, 15, 10]. The lattice spacing of CD was 0.32 nm which well agrees with the plane (002) spacing of carbon as already mentioned in **Chapter 4** [2, 9]. Elemental compositions of CD@TiO_2 were determined from EDX data (**Figure 6A.1g**). The weight and atomic ratios of C, N, O and Ti in CD@TiO_2 were found to be 23.8:9.5:38.9:27.6 and 34.9:12.0:42.8:10.1. Again, TEM images of CD/TiO_2

also showed that TiO_2 nanoparticles are slightly rod like in shape and also well-dispersed on CD surface (**Figure 6A.2a**).

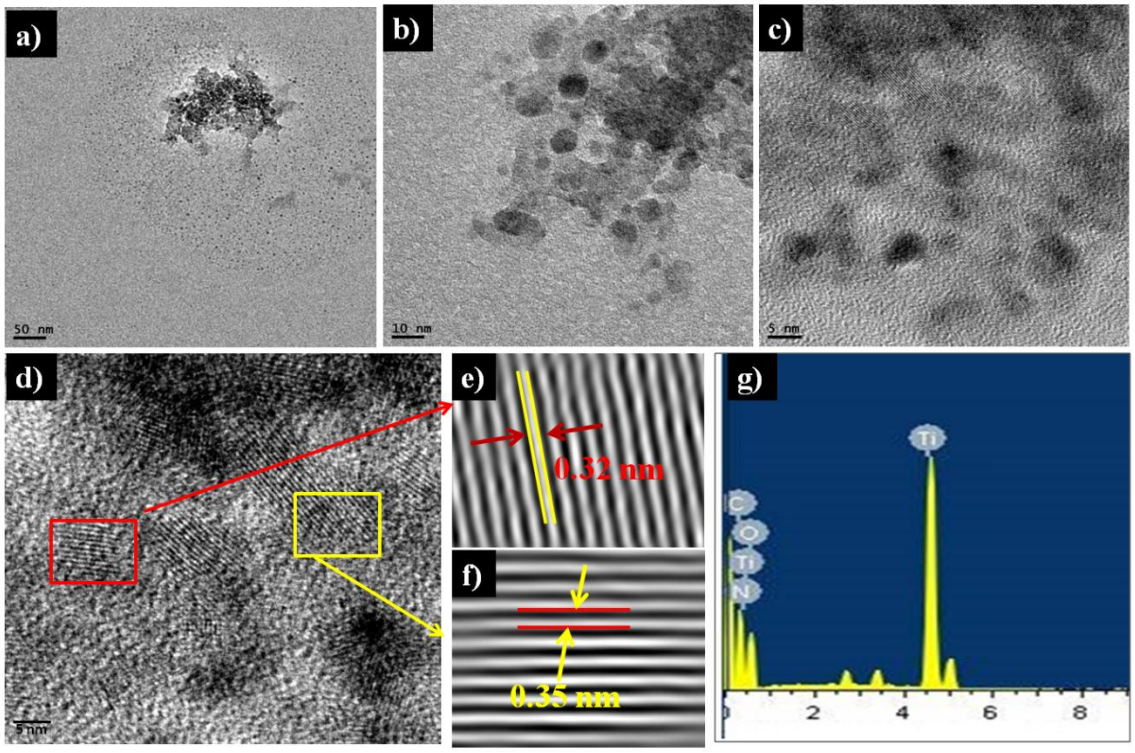

Figure 6A.1: TEM images of CD@TiO_2 at **(a)** 50 nm, **(b)** 10 nm, **(c)** 5 nm and **(d-f)** lattice fringes of TiO_2 and CD, and **(g)** EDX map of CD@TiO_2

SEM was used to measure the surface morphology of TiO_2 nanoparticles, CD/TiO_2 and CD@TiO_2 nanohybrids (**Figure 6A.2b and 6A.3**). It is seen from SEM images of CD/TiO_2 (**Figure 6A.2b**) that the nanohybrid is agglomerated and hence, it is difficult to obtain the exact morphology of it. In bare TiO_2, TiO_2 nanoparticles were nanorod in shape. But after the formation of nanohybrid with CD (CD@TiO_2), the shape TiO_2 was changed to nearly spherical with uniform distribution (**Figure 6A.3**).

Further, rough nanostructural surface was observed in case of nanohybrid (**Figure 6A.4**). This was confirmed from 3D surface plot of the nanohybrid by plotting with the help of Fiji ImageJ software.

The presence of different functional groups on the surface of bare TiO_2, CD@TiO_2 and CD/TiO_2 were confirmed from FTIR spectroscopic studies (**Figure 6A.5a**). In the FTIR spectrum of bare TiO_2, absorption band at 3401 cm^{-1} is attributed to -O-H stretching, 2923 cm^{-1} and 2852 cm^{-1} are assigned to -C-H asymmetric and symmetric stretching and band at 1410 cm^{-1} is due to stretching

vibration of -Ti-O-Ti group. The board band emerges in a range of 700-500 cm^{-1} is due to bending vibration of Ti-O bond in TiO_2 lattice. The band observed at 1628 cm^{-1} is assigned to molecular water bending mode.

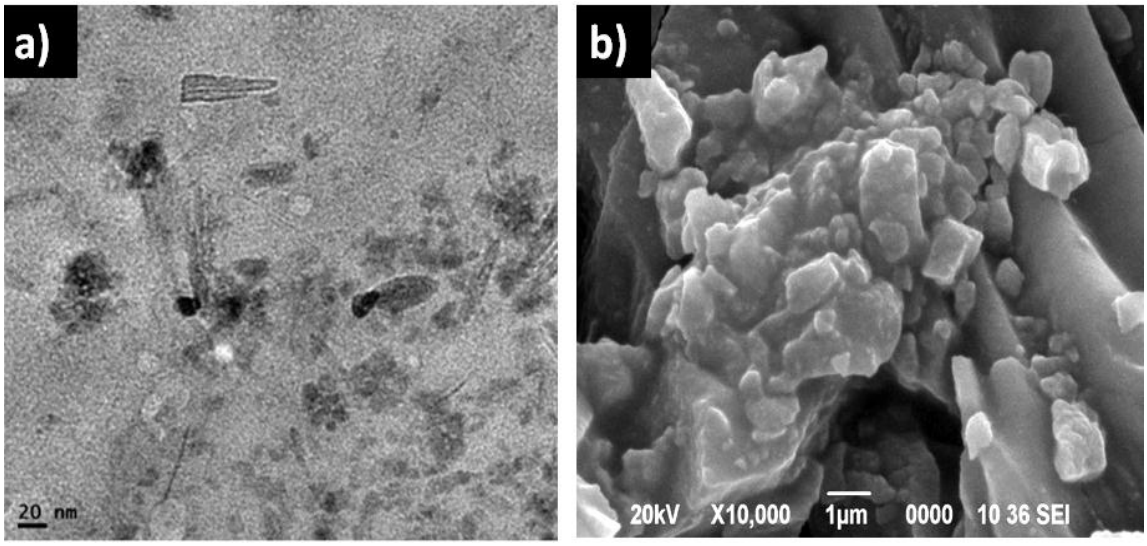

Figure 6A.2: (a) TEM and **(b)** SEM images of CD/TiO_2

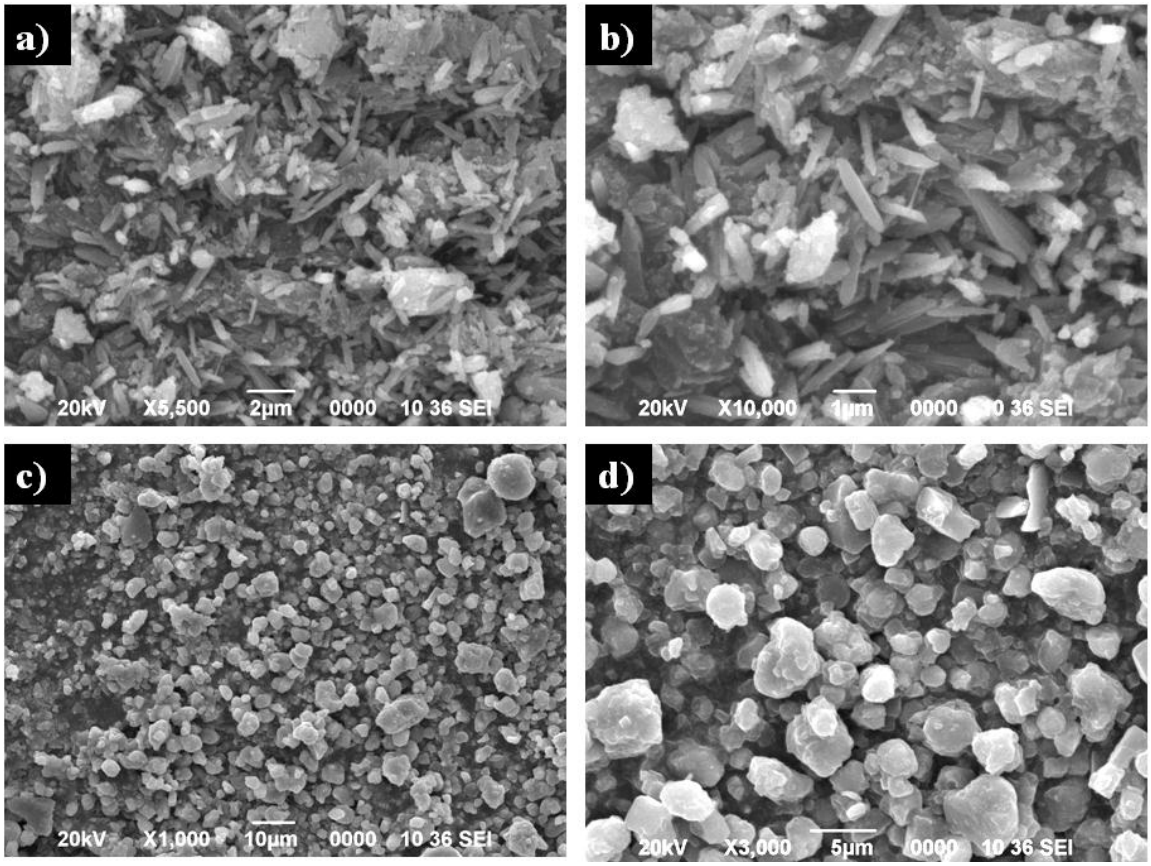

Figure 6A.3: SEM images at two different magnifications **(a**, **b)** for bare TiO_2; and **(c**, **d)** for CD@TiO_2 nanohybrid

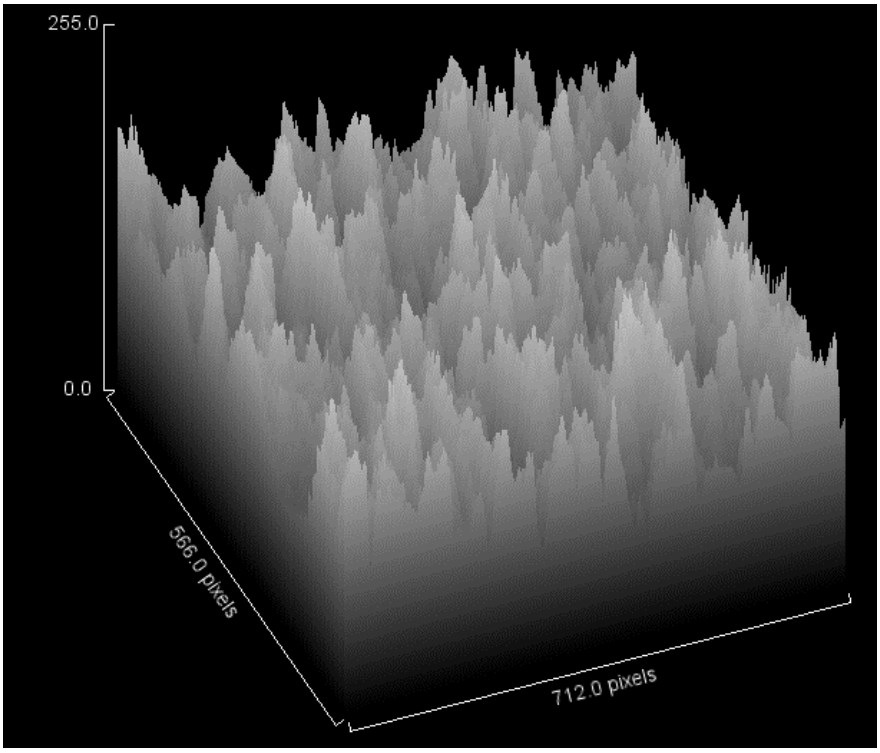

Figure 6A.4: 3D Surface plot of the nanohybrid

The band appeared at 720 cm^{-1} is ascribed to superficial Ti-O vibrations for TiO_2. In the FTIR spectrum of CD@TiO_2, -O-H absorption band was shifted to 3435 cm^{-1}[21, 22]. The absorption band at 1628 cm^{-1} in the nanohybrid decreases with the increase in temperature of synthetic process, which indicates that surface hydroxyl groups enable the condensation under hydrothermal condition.

X-ray diffraction (XRD) patterns of bare TiO_2, CD@TiO_2 and CD/TiO_2 are shown in **Figure 6A.5b**. XRD pattern of bare TiO_2 showed peaks of 2θ values at 25.3, 37.7, 48.0, 54.2, 55.6, and 62.8° are assigned to the (101), (004), (200), (105), (211) and (204) planes of anatase TiO_2, respectively. CD@TiO_2 nanohybrid also showed XRD peak for anatase structure of TiO_2. But the XRD pattern of CD/TiO_2 showed the presence of both anatase and rutile forms of TiO_2 as denoted by 2θ peaks at 25.4 and 62.7° corresponding to (101) and (204) planes of anatase phase and peaks at 27.57, 36.21, 41.37, 54.45, 56.76, and 69.12° corresponding to the (110), (101), (111), (211), (220) and (112) reflection planes of rutile phase, respectively. This confirmed the crystalline nature of the synthesized particles [11, 15, 19]. The results of XRD studies for CD@TiO_2 and CD/TiO_2 reflect that the structure of TiO_2 nanoparticles is greatly influenced by the mode of formation, particularly the presence of *in-situ* generated CD or preformed CD.

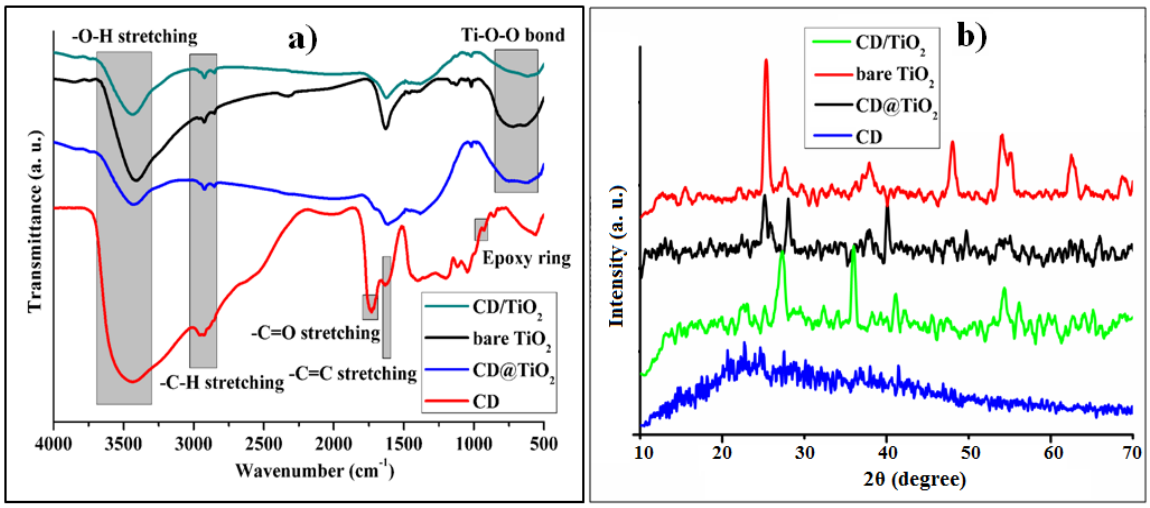

Figure 6A.5: (a) FTIR spectra and **(b)** XRD patterns of the nanomaterials

TG analyses were carried out to investigate the thermal behavior of the nanomaterials. The TG thermograms and DTG curves of bare TiO_2, CD@TiO_2 and CD/TiO_2 are shown in **Figure 6A.6**. TG thermograms of bare TiO_2 and CD/TiO_2 showed two step degradation patterns. The first step degradation of TiO_2 was observed in the range of 50-150 °C, which is due to loss of absorbed water molecules or other volatiles. The second step degradation at around 200-600 °C is attributed to removal of organic residue trapped inside the pore and degradation of adsorbed components on the surface of nanomaterials [23, 24].

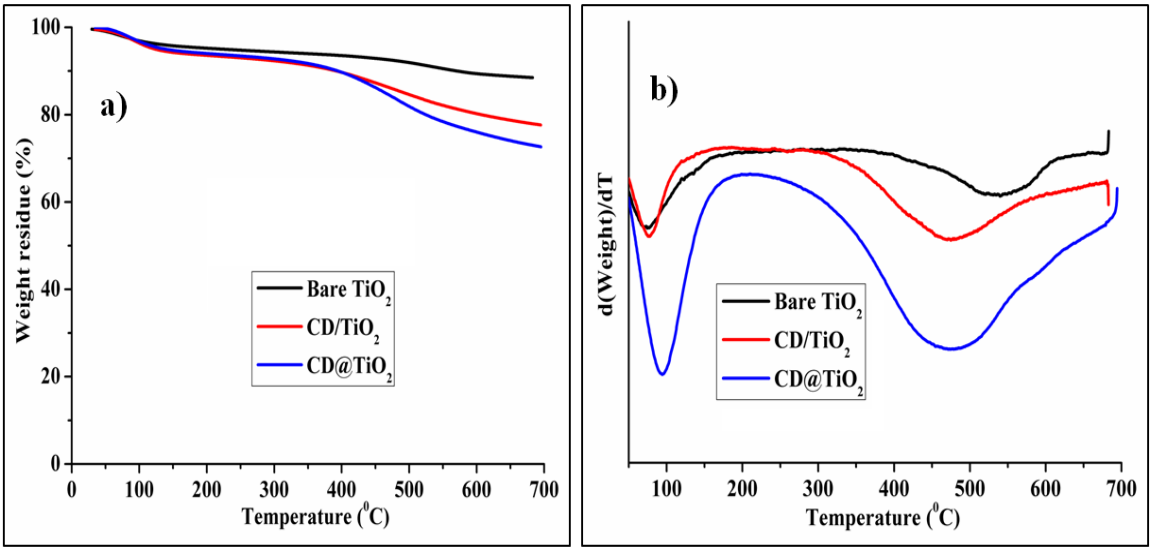

Figure 6A.6: (a) TG thermograms and **(b)** DTG curves of bare TiO_2, CD/TiO_2 and CD@TiO_2

6A.3.3. Optical properties

The optical properties of the nanomaterials were studied by UV-visible and fluorescence spectral analyses. TiO_2 nanoparticles exhibit a broad absorption band from 200 to 400 nm (**Figure 6A.7a**), indicating the effective photo-absorption, which is useful to its photocatalytic property. While, CD@TiO_2 showed an efficient absorption in the visible region implies its good photocatalytic ability under visible light [21, 22]. Thus, CD@TiO_2 nanohybrid expected to exhibit higher photocatalytic activity than that of bare TiO_2 nanoparticles [11, 19]. In PL spectra (**Figure 6A.7b)**, the maximum emission peaks of CD@TiO_2 were shifted from 420 to 560 nm with the increase of excitation wavelengths from 340 to 460 nm. It was also observed that the nanohybrid demonstrated excitation wavelength dependent down-conversion PL emission. This is due to the existence of different surface states and size dispersion of the nanomaterials. They also possess excellent up-conversion fluorescence. With the exciting wavelengths from 650 to 800 nm, the corresponding up-conversion emission spectra appeared from 420 to 525 nm (**Figure 6A.7c**).

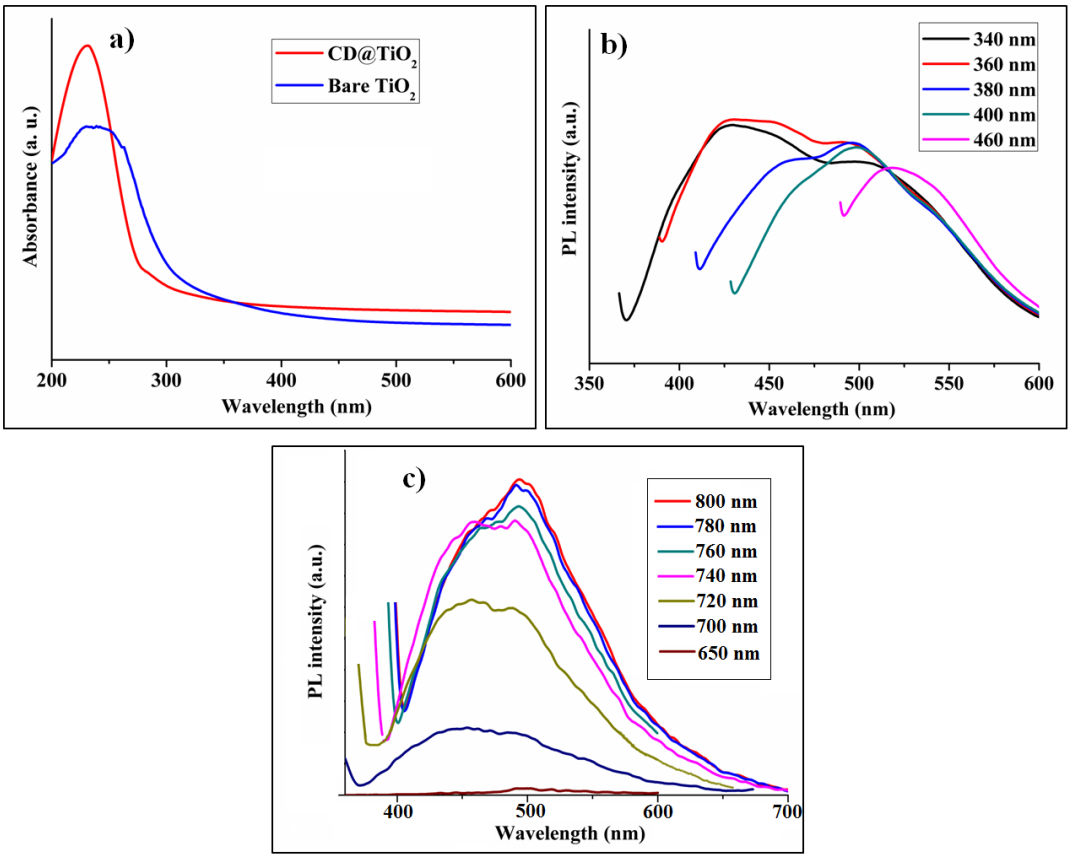

Figure 6A.7: (a) UV-vis spectra of bare TiO_2 and CD@TiO_2, and wavelength dependent **(b)** down- and **(c)** up-conversion PL spectra of CD@TiO_2

This characteristic may be attributed to the different emissive sites on each CD, distribution of different particle sizes of CD and the multiphoton active processes [25, 26]. Another cause for the excitation dependent PL behavior of CD is surface chemistry. The presence of different types of functional groups on the surface of CD may produce different emissive traps between π and π* of C=C. The self-passivated nitrogen and oxygen containing functional groups on CD surface may be responsible for the efficient PL by trapping excitons under excitation and the radiative recombination of those surface trapped excitons. CD on illuminating at a certain excitation wavelength a surface energy trap dominates the emission. The other corresponding surface state emissive traps become dominant as the excitation wavelength changes. Thus, the mechanism of PL is controlled by both surface defects and size effects [23, 25].

6A.3.4. Photocatalytic degradation

The photocatalytic activity of semiconductor is a result of the production of excited electrons under UV irradiation in its conduction band along with corresponding positive holes in the valence band, which react with contaminants adsorbed on the photocatalyst surface. However, the relatively large band gap of TiO_2 reduces the efficiency of photocatalytic reactions due to high recombination rate of photogenerated electrons and holes formed in the photocatalytic process and low absorption capability of visible light [11, 19]. In CD@TiO_2 and CD/TiO_2, the presence of CD reduced the e^-/h^+ recombination rate and hence the efficiency of the photocatalyst was increased. Also, the presence of nitrogen in CD@TiO_2, keeps a good control of the main particle size to produce nanoscale configuration of the catalyst. CD@TiO_2 showed higher degradation than CD/TiO_2 because in CD@TiO_2 nanohybrid, TiO_2 is in anatase form, whereas in CD/TiO_2 nanohybrid, TiO_2 is in both anatase and rutile forms. The photocatalytic activity of TiO_2 is strongly dependent on its crystallite size, phase structure, pore structure and specific surface area. Because of larger band gap (3.2 eV) of anatase than that of rutile (3.0 eV), anatase has lower absorbance ability towards solar light than rutile, the photocatalytic activity of anatase is apparently superior to that of rutile. This is due to the reason that anatase possesses a lower charge carrier recombination rate and higher surface adsorption capacity to hydroxyl groups than rutile. The lower photocatalytic activity of rutile is due to larger size, having inferior surface adsorption capacity and lower specific surface area. Besides this compared to rutile phase in anatase the lifetime of photogenerated electrons and holes is about an order of magnitude higher and thus

greatly enhancing the chance of photoexcited holes and electrons in anatase participating in surface chemical reactions [4, 11, 19]. Hence, the 'as synthesized' CD@TiO_2 showed better photocatalytic activity towards pesticide, phenol and benzene compared to CD/TiO_2 nanohybrid, bare TiO_2 and CD (**Figure 6A.8 and Figure 6A.9**).

The kinetics of photocatalytic degradations of pesticide, phenol and benzene have been studied in terms of Langmuir-Hinshelwood (L-H) rate equations. L-H rate expression has been effectively applied for heterogeneous photocatalytic degradation to determine the correlation between the initial degradation rate and the initial concentration of the organic substrate by the following equation [27-30].

$$1/K = 1/ k_c K_{LH} + [C]_0/k_c \quad \text{.....} \quad \textbf{6A.1})$$

where $[C]_0$ is the initial concentration of organic compound (mg L^{-1}), K_{LH} the Langmuir-Hinshelwood adsorption equilibrium constant (L mg^{-1}) and k_c is the rate constant of the surface.

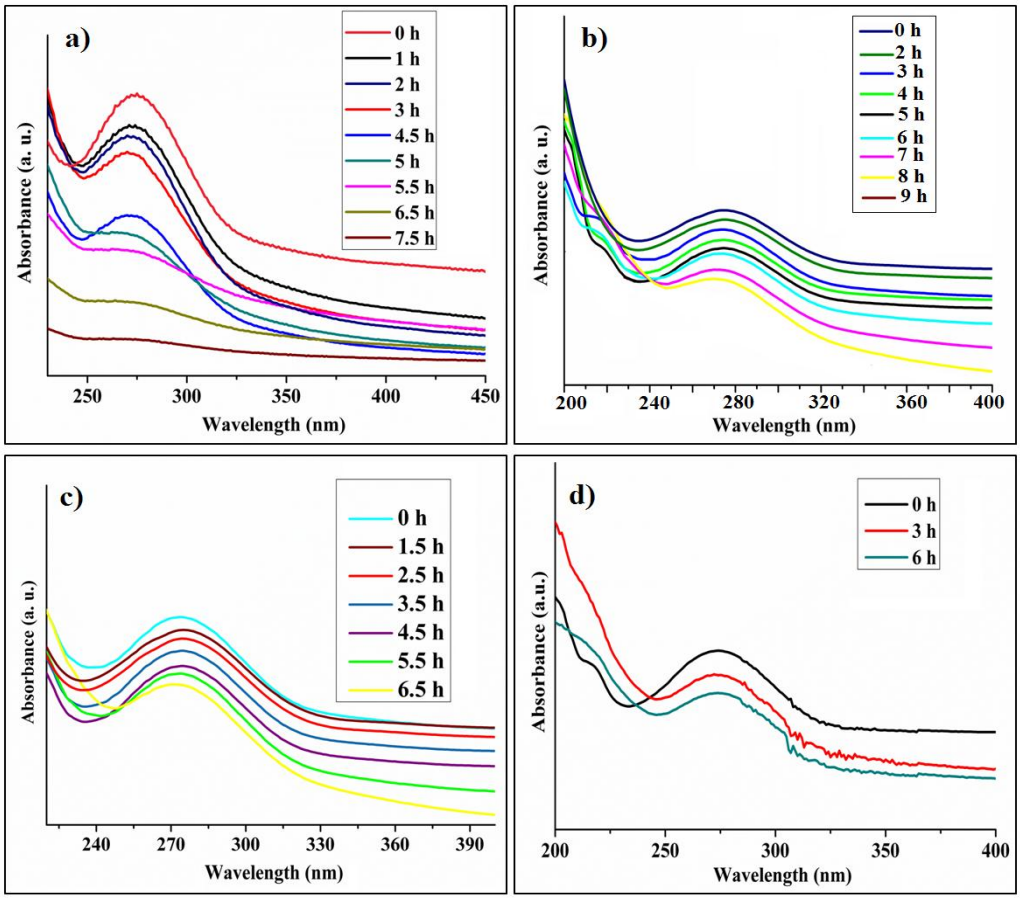

Figure 6A.8: Plots of UV absorbance against wavelength for degradation of paraoxon pesticide at different times in presence of **(a)** CD@TiO_2, **(b)** CD/TiO_2, **(c)** CD and **(d)** bare TiO_2 nanomaterials

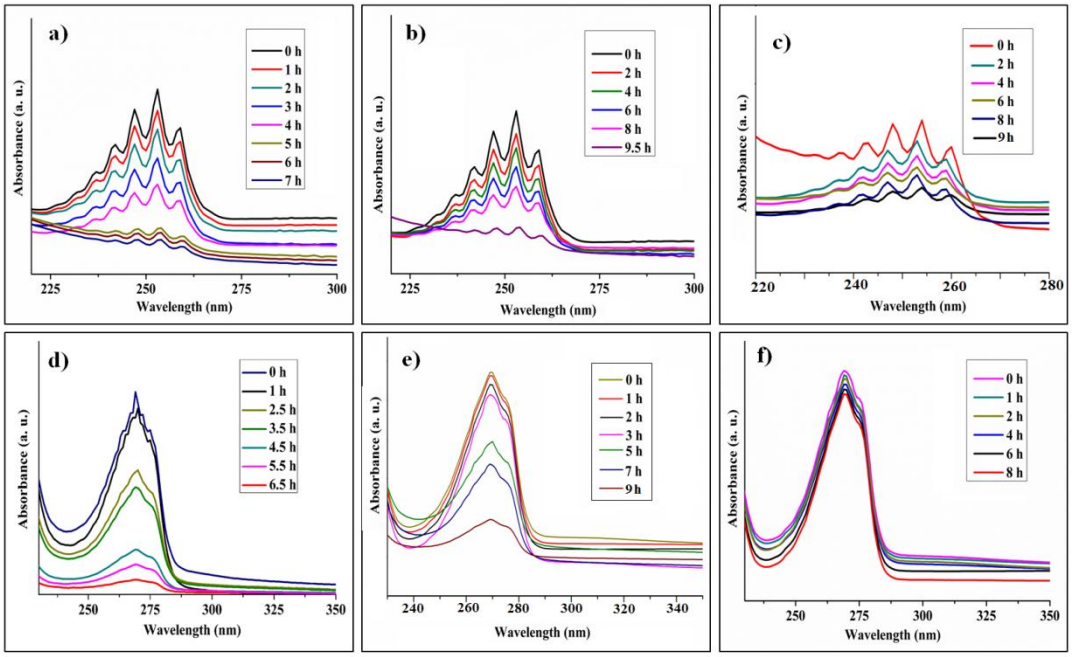

Figure 6A.9: Plots of UV absorbance against wavelength for degradation of **(a-c)** benzene and **(d-f)** phenol at different times in presence of CD@TiO$_2$, CD/TiO$_2$ and bare TiO$_2$ nanomaterials respectively

The degradation of these organic pollutants and pesticide containing CD@TiO$_2$ follows the pseudo-first-order kinetics with respect to the concentration of them in the bulk solution (C) [28, 29].

$$r = -dC/dT = k_{obs}C \quad \text{(Eq. 6A.2)}$$

Integration of the above equation (with respect to $C=C_o$ at t=0, where C_o is the initial concentration and t is the reaction time) gives the following expression

$$\ln(C_0/C) = k_{obs}Ct \quad \text{(Eq. 6A.3)}$$

where k_{obs} is the apparent pseudo-first-order rate constant which is affected by concentration of organic pollutants.

Photocatalytic degradations of paraoxon pesticide, benzene and phenol were studied by CD, bare TiO$_2$, CD@TiO$_2$ and CD/TiO$_2$ under normal solar light. The rates of degradation of pesticide, phenol and benzene with time for CD@TiO$_2$ and CD/TiO$_2$ are presented in **Figure 6A.10**. From these figures, it is clear that the time taken for 90% degradation of the pesticide was 7.5 h by CD@TiO$_2$, whereas only 70% degradation of the same by CD/TiO$_2$ was observed after 9 h under the same solar light. Again, a little degradation was observed for bare CD and TiO$_2$ even after 6 h. Similarly, for 90% degradation of the benzene, the time taken by CD@TiO$_2$ was 7 h, whereas only 60%

degradation of the same by CD/TiO_2 was observed after 9.5 h. On the other hand, bare TiO_2 nanoparticles degrade benzene to a small extent even after 9 h. The degradation efficiency for benzene by CD@TiO_2 is much higher compared to the reported CD based nanohybrids like Fe_2O_3/CD and ZnO/CD. The degradation efficiency for the latter cases was only 80% and 86% respectively even after visible light irradiation of 24 h [10, 11]. Further, the same degradation by TiO_2/MWCNT was only possible by exposure of UV light [19]. However, the time taken for 93% degradation of the phenol was 6.5 h by CD@TiO_2, whereas CD/TiO_2 degraded the same upto 65% after 9 h, and bare TiO_2 exhibited only slight photocatalytic activity for phenol degradation even after 8 h. On the other hand, CD showed no degradation even after 8 h. The photocatalytic activity of the synthesized CD@TiO_2 nanohybrid towards phenol was also found to be much higher than the reported Fe/TiO_2 nanohybrid, where the latter showed only 65.68% degradation. The nanohybrids like Fe/TiO_2 and MWNT/TiO_2 degraded phenol but the exposure of UV light is must in both the cases [20, 16]. The fitting plots of ln (C_0/C) *vs* time for CD@TiO_2 and CD/TiO_2 are shown in **Figure 6A.10** and demonstrated that the degradations of benzene and phenol are well described by first order kinetics with the fitting coefficients over 0.9, indicating photo-degradation behavior.

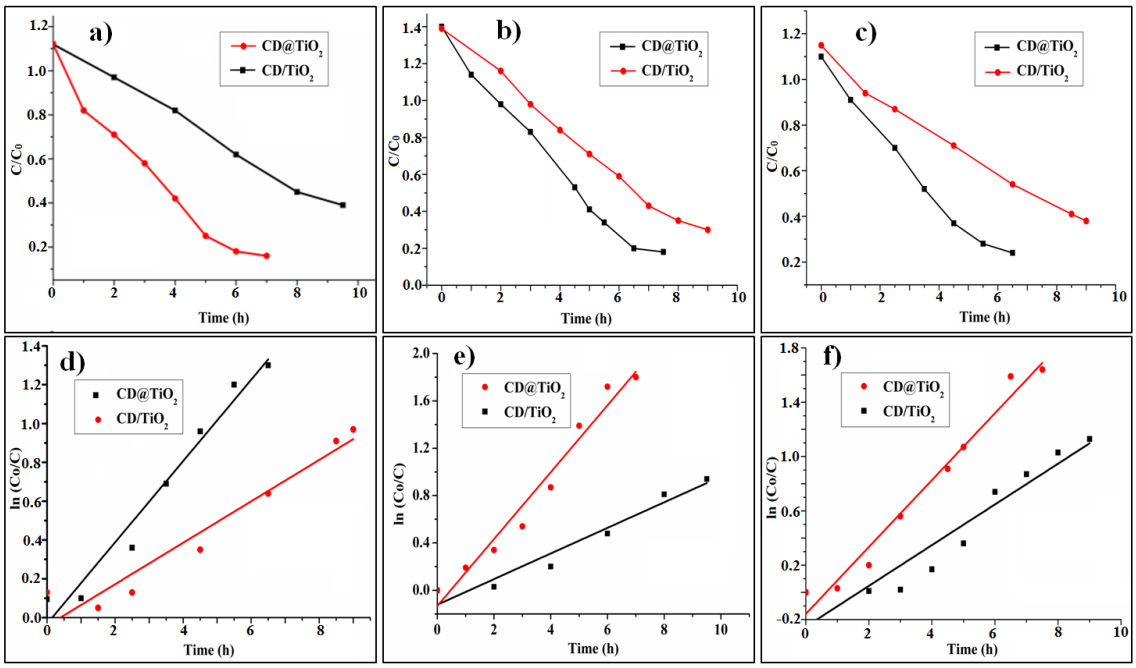

Figure 6A.10: Degradation curves of aqueous solution of **(a)** benzene, **(b)** pesticide and **(c)** phenol and fitting degradation kinetic curves for **(d)** benzene, **(e)** pesticide and **(f)** phenol by TiO_2 nanohybrids

The degradation of paraoxon pesticide also follows pseudo first order kinetics with the fitting coefficients over 0.97 and 0.94 by CD@TiO_2 and CD/TiO_2, indicating regular photo-degradation behavior. Though bare TiO_2 nanoparticles degrade pesticide but their efficiencies are very poor due to their high recombination rate of photogenerated e^-/h^+ pairs. However, it is only useful under exposure of UV light which hinders their practical applicability. Though literature also reported the degradation of the pesticide, benzene and phenol using different nano photocatalysts, but in almost all the cases the photocatalytic degradation was studied under UV irradiation. Further, the catalytic activity of these catalysts is inferior compared to the presently reported CD@TiO_2 nanohybrid, where other than normal solar light no additional energy is needed.

The photocatalytic degradation of phenol at three different initial concentrations (10, 30 and 50 mg) was studied as a representative example to determine the value K_{LH} and k_C. The initial concentration of phenol has a fundamental effect on the rate of degradation, i.e. with the increase of the initial concentration of phenol, the kinetic rate constant decreases. The plot of ln(C_0/C) *vs* t for degradation of phenol with different initial concentrations is shown in **Figure 6A.11a** and from the regression analysis of this linear plot, the values of k_{obs} can be obtained. The values of k_{obs} and the regression coefficients with respect to different initial concentrations are tabulated in **Table 6A.1**. From the above table, it is noticed that the first order reaction is better agreed with lower concentrations of phenol.

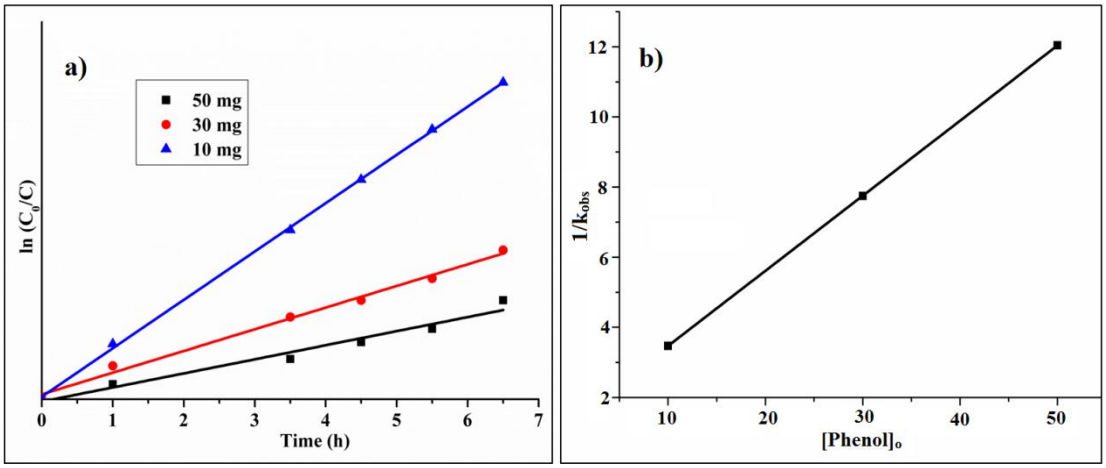

Figure 6A.11: (a) Plot of ln (C_0/C) *vs* time for photocatalytic degradation of phenol at three different concentrations of phenol and **(b)** variation of reciprocal of rate constant *vs* different initial concentrations of phenol

The plot of $1/k_{obs}$ *vs* $[C]_0$ of phenol is shown in **Figure 6A.11b** which showed a linear variation according to **Eq.6A.1**. From this, it is confirmed that the Langmuir-Hinshelwood relationship is valid for the initial rates of degradation [28]. The values of K_{LH} and k_c, calculated from the slope and intercept of the straight line (R^2=0.99) were found to be 0.214 $mgL^{-1}$and 1.325 $mgL^{-1}h^{-1}$.

Table 6A.1: Pseudo first order rate constant at different initial concentrations of phenol

C_0 (mgL^{-1})	$K_{obs} \times 100$ (min^{-1})	R^2
10	0.48	0.999
30	0.22	0.991
50	0.14	0.963

Based on other reported CD/metal and/or metal oxide nanoparticles by exploiting the up-conversion fluorescence properties of CD photodegradation mechanism is schematically shown in **Scheme 6A.2.**

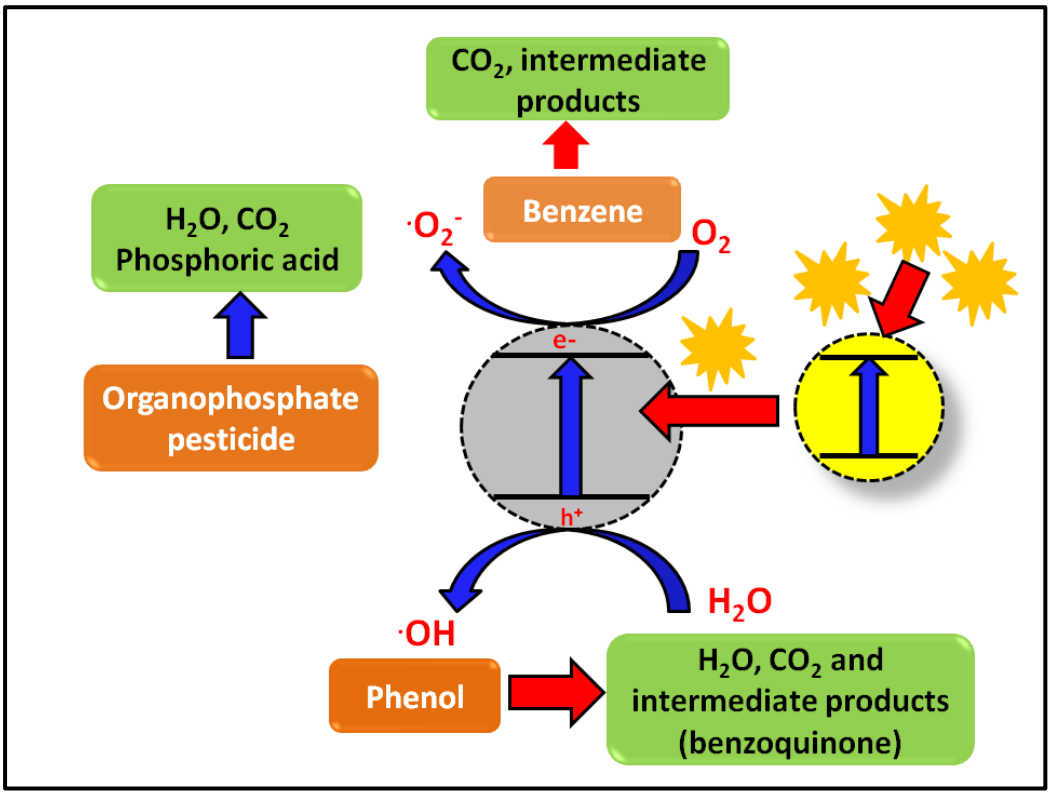

Scheme 6A.2: Photocatalytic mechanism for pesticide, benzene and phenol by CD@TiO_2 nanohybrid

CD present in CD@TiO_2 nanohybrid plays two crucial roles for enhancing the photocatalytic activity of TiO_2. One of them is to act as an electron reservoir that helps to trap electrons emitted from TiO_2 nanoparticles due to irradiation by normal sunlight, therefore hindering recombination rate of e^-/h^+ pairs. In addition, CD also acts as a dispersing support to control the morphology of TiO_2 in CD@TiO_2 nanohybrid, in other words, it prevents agglomeration of as-synthesized TiO_2 [19]. When CD was loaded on the surface of TiO_2, the relative position of the CD band edge allows the transfer of electrons from the TiO_2 surface, permitting charge separation, stabilization, and hindered recombination. The electrons can be shuttled freely along the conducting network of CD, while hole stays electronically and structurally near TiO_2. This process can effectively hinder the e^-/h^+ recombination, and thereby enhancing the reactivity of photogenerated electron and hole generated on exposure of visible light. Then, the oxygen radicals ($^{\bullet}O_2^-$) would be formed by the combination of electrons in the conducting network of CD with O_2, adsorbed on the surfaces of CD. When CD@TiO_2 was exposed under solar light, CD absorbs visible light, and emits shorter wavelength of light (325-425 nm) as a result of up conversion. This is in turn excites TiO_2 to form e^-/h^+ pairs and they react with H_2O and O_2 to produce reactive oxygen species like $^{\bullet}OH$, $^{\bullet}O_2^-$ which subsequently cause degradation of phenol, paraoxon pesticide and benzene [9-11, 18, 19]. CD@TiO_2 also absorbs more visible light compared to CD as revealed from absorption spectra (**Figure 6A.7a**), which helps to increase the catalytic efficiency of CD@TiO_2 under solar light. The products form after degradation of the pesticide are H_2O, CO_2, phosphoric acid, N_2, O_2 etc., as reported in literatures [18]. In degradation of phenol, $^{\bullet}OH$ can react with phenol and producing intermediate products like benzoquinone. These products can further react with another $^{\bullet}OH$ or hole to produce CO_2 and H_2O. During the degradation of benzene, the π–π^* interaction between the benzene and conjugated structure of CD is beneficial for the enhancement of benzene on the surface of CD@TiO_2 nanohybrid [10, 11]. All those above mentioned effects are together responsible for the enhanced photocatalytic activity of CD@TiO_2 compared to CD/TiO_2 nanohybrid, bare TiO_2 and CD nanoparticles.

6A.4. Conclusion

Thus, the study demonstrated a facile, green and eco-friendly one pot synthesis of CD@TiO_2 by utilizing carbon precursors (citric acid, glycerol and cow urine) and

titanium butoxide. The nanohybrid, CD@TiO_2 also exhibited excellent excitation wavelength dependent down- and up-conversion fluorescence behaviors. Furthermore, CD@TiO_2 showed the highest and most efficient photocatalytic activity towards organic pollutants like phenol and benzene, and pesticide compared to bare CD, TiO_2 and CD/TiO_2. Therefore, it can be asserted that this kind of environmentally friendly and highly luminescent CD@TiO_2 nanohybrid may open up a new avenue for its practical applications as a photocatalyst for efficient and economical remediation of different pollutants towards safe and sustainable environment.

6B.Fabrication of WHPE/CD@TiO_2-based nanocomposite

6B.1. Introduction

The previous chapters addressed the development of WHPE nanocomposite with adequate performance including mechanical and thermal properties along with good adsorption and photocatalytic activity using CD@clay nanohybrid. However, some special properties like anti-reflecting, anti-fogging, anti-icing are lacking in the above nanocomposites. Thus, in this study, in order to explore some unique multi-faceted properties like self-cleaning, anti-reflecting, antibacterial activity, anti-fogging, anti-icing, etc. as well as to increase the photocatalytic activity of the nanocomposite, an attempt was made to incorporate TiO_2 in WHPE system as it is a very good photocatalyst. Literature reports that incorporation of it into different polymer matrices like epoxy [31], polyurethane [32], polyester [33, 34], poly(ester urethane) [35], polyamide [36], poly(methyl methacrylate) [37], etc. results not only improvement in mechanical, thermal, etc. properties but also imparts unique and useful attributes to the resultant nanocomposites due to some special characteristics of it as mentioned in the above sub-chapter which are unattainable both by CD and CD@clay-based WHPE nanocomposites [32-35]. TiO_2 is also used to achieve high thermostability, delay heat conduction, provides high free energy barrier for ice nucleation along with improvement of mechanical and thermal properties. Further, it can provide roughness to the organic polymer surface due to inherent incompatibility as it is an inorganic material. All of these are the essential requirement for achieving properties like anti-icing, anti-fogging, oil-water separation, etc. Advanced materials with such unique multi-functional activities are the ultimate choice of the material community, as they not only assist economy of the country but also help to conserve the exhaustible resources [38]. In recent times, fabrication and designing of anti-fogging and anti-reflecting surfaces are very essential for using in an array of applications such as displaying devices, display screens, solar cells, lenses, all types of optical and optoelectronic devices. In addition, research on anti-icing surfaces is also very important as accumulation and adhesion of ice lead to major problems to individual daily life such as communicating destruction, traffic interruption, damages of equipments related to electricity, telecommunication and transportation, loss of power, etc. Further, polymeric surfaces with self-cleaning property are of industrial and academic interest, as it can save cost of maintenance and lot of time [39-41]. TiO_2 nanoparticles have also been reported to possess board spectrum of antibacterial activity

against microorganisms including gram-negative and gram-positive bacterial strain as well as fungi. Thus, antibacterial nanocomposites based on TiO_2 have been actively investigated in recent years. These nanocomposites can exhibit non-contact biocidal action as well as they may inherently environmentally friendly [42, 43]. Biocidal action is a result of modulation of electron/hole (e^-/h^+) pairs at the interface of the material upon photoactivation and dispersion of inorganic as well as organic-inorganic interfacial contact yields strong and long-term such capability. They possess significant advantages over both metal (usually Ag) and chemical (H_2O_2, NO, small organic molecules)-based biocides. However, achieving of these properties simultaneously in polymeric materials is rare to find in literature and hence, it is a daunting challenge to endow the combined properties in a single material. In addition, so far no report was found on fabrication of thermosetting TiO_2-based WHPE nanocomposite. Further, the studies on polyester/TiO_2 nanocomposites reported in literature are not comprehensive and systematic. Ghanem *et al.* [34] reported fabrication of hyperbranched polyester nanocomposite using TiO_2 by both *in-situ* and *ex-situ* methods but studied only photocatalytic activity. While Zhang *et al.* [44] studied only the thermal properties of copolyester/TiO_2 nanocomposites. Similarly, Santos *et al.* [33] studied only the thermal properties and hardness of the nanocomposites of poly(ethylene terephthalate) and TiO_2. Therefore, all the above cited reports are lacking to address the above unique properties. In addition, they were obtained from petroleum resources and solvent borne systems were used. Both of these are against the tenets of green chemistry as well as unable to maintain the concept of triple bottom line approach. As these are the central requirements for any kind of sustainable development, so an environmentally benign facile approach like waterborne system and renewable resources, is the most desirable approach to be adopted because of their advantages as mentioned in **Chapter 1** [45, 46]. Further, only bare TiO_2 may have the compatibility problem with polyester as it does not possess as such any suitable functionality to interact with such matrix. In addition, bare TiO_2 leads to the formation of aggregates due to the high surface energy, thus making them poorly dispersed into the matrix [31-34]. Thus, a nanohybrid of TiO_2 with CD was synthesized in the previous sub-chapter by a single pot one step facile protocol and proposed to use for fabrication of WHPE nanocomposite. CD helps in dispersion and stabilization of TiO_2 as well as enhances its photocatalytic activity due to the favorable electron transportation and charge mobility properties of it [32, 33]. It is pertinent to mention here that even though

this nanohybrid is reported in literature but no report was found so far on incorporation of such nanohybrid in WHPE system.

Therefore, the present study demonstrates the fabrication of an environmentally benign multi-functional WHPE/CD@TiO_2 nanocomposite using bio-based raw materials for the first time through a benign *in-situ* polymerization method. Glycerol based hyperbranched epoxy (HBGE) and fatty acid based poly(amido amine) (PAA) modified above nanocomposite was evaluated as a tough polyester thermoset. The fabricated thermosetting nanocomposites with different wt% of nanohybrid were examined as multipurpose advanced sustainable polymeric materials with special attributes like anti-reflecting, anti-icing, anti-fogging, self-cleaning, etc. This material was also tried to use as a membrane for separation of oil and water from their mixture, and as a photocatalyst for reduction of 4-nitrophenol (4-NP) under normal sunlight.

6B.2. Experimental

6B.2.1 Materials

In this study, WHPE50 was used as the matrix for fabrication of the nanocomposite like the previous chapter. Thus, same materials and method were used related to WHPE50 as described in **sub-Chapter 2B, sub-section 2B.2**. Bare TiO_2 nanoparticles and CD@TiO_2 nanohybrid used for fabrication of nanocomposites were prepared by the same method using the same materials as described in the previous sub-chapter. All other materials like solvents, HBGE, PAA, etc. used in this study were same as described in **sub-Chapter 2A**. Methylene blue (MB) used for photocatalytic test was the same as mentioned in **Chapter 4**. Phenol and ethyl paraoxon pesticide used in this study was the same as described in the **sub-chapter 6A.1**. Methyl orange (MO) and bisphenol A (BPA) were obtained from Merck, India and SRL, India respectively. These are used in this study for photocatalytic test. 4-NP was purchased from Sigma Aldrich, Germany and used in this study for performing the photocatalytic reduction test.

6B.2.2. Characterization

The characterization and instrumentation methods including microscopic, spectroscopic, diffraction, mechanical and thermal were the same as mentioned in **Chapter 3**. The transmittance percentages of the nanocomposite films were evaluated using the same instrument as mentioned **Chapter 4**. Further, the optical color emission photos and PL

properties of the nanocomposites were recorded using the same instrument as described in **Chapter 4**.

6B.2.3. Fabrication of WHPE/CD@TiO_2 nanocomposite

WHPE nanocomposites were fabricated using nitrogen containing CD@TiO_2 through a facile *in-situ* method without using catalyst, neutralizing agent and organic solvent. The first step of fabrication process was the same as described in **sub-Chapter 2A, sub-section 2A.2.4**. After cooling this reaction mixture to 60 °C, required amount of bis-MPA and glycerol was added into it along with the desired amount of CD@TiO_2 nanohybrid and again the reaction was carried out at 140 °C. Then, by following the same preparative protocol, three different nanocomposites were fabricated using 0.5, 1 and 2.5 wt% CD@TiO_2 and denoted as PCTN0.5, PCTN1 and PCTN2.5 respectively. The nanocomposites of polyester with bare TiO_2 (1 wt%) was also prepared for comparison purpose and coded as PTN1.

6B.2.4. Preparation of the thermosets

The thermosets of this nanocomposite was obtained by following the same procedure as described in **sub-Chapter 2A, sub-section 2A.2.3**.

6B.2.5. Anti-reflecting test

The anti-reflectance property of the nanocomposite films was investigated by measuring the transmittance, T (%) of them with the help of a UV-vis spectrophotometer.

6B.2.6. Anti-fogging test

Anti-fogging ability of the coated films was tested by holding them at low temperature in a cold chamber (-20 ^oC) for 1 h, followed by returning to ambient conditions for the formation of moisture drops. Photographs were then recorded in each case. The transparency of the coated surface under the fogging or frosting conditions was also evaluated to examine the anti-fogging behavior of the nanocomposite films.

6B.2.7. Anti-icing test

The anti-icing behavior of the nanocomposite films was tested by pouring cooled water droplet (-15 ^oC) onto the chilled surfaces of the coated and bare glass and aluminium

plates with help of a syringe and kept under freeze condition for 5 min. The photographs of water drops were taken immediately.

6B.2.8. Photocatalytic activity

6B.2.8.1. Self-cleaning test by photocatalytic degradation

Self-cleaning test was done by monitoring the photocatalytic degradation of four organic contaminants such as mixed dye (MB and MO), phenol, BPA and ethyl paraoxon pesticide under normal sunlight. For this experiment, the nanocomposite films were cut into small pieces and taken in aqueous solution of the contaminants. In a typical procedure, (1-2 g) of nanocomposite film containing 25-50 mg CD@TiO_2 was taken in 50 mL aqueous solution of mixed dye (10 ppm) or BPA (30 ppm) or phenol (20 ppm) or pesticide (10 ppm). The solution was stirred in the presence of nanocomposite films under the normal sunlight. The degradation of organic contaminants was observed by detecting the UV absorbance intensity at wavelength of 300-600 nm for the specified period of time. A fixed amount of sample was withdrawn from this stock solution at regular intervals and the characteristic absorbance was measured. The same experiment was done for all the nanocomposites. The photocatalytic activity of the films was calculated from the rate of change of contaminant concentration with exposure time. To study the recyclability of the films, the used pieces in the first cycle were recovered by normal filtration after obtaining the maximum extent of degradation of contaminant and the weight of the films was taken after drying. These dried films were further used for the subsequent cycle. The degradation efficiency was calculated by following the same equation as mentioned in **Chapter 4**.

6B.2.8.2. Reduction of 4-NP

The photocatalytic activity of the nanocomposite was tested by the reduction of 4-NP by the nanocomposite film under normal sunlight. In a typical procedure, freshly prepared aqueous solution of 4-NP (20 mL, 1 M) was mixed aqueous solution of $NaBH_4$ (2 mL, 0.05M) in a 50 mL round bottom flask. The small pieces of nanocomposite film (5 mg) was added into the above reaction mixture and then exposed to normal sunlight. The addition of this film to the reaction mixture initiates the reduction process. The change in the absorbance intensity was monitored by a UV-vis spectrophotometer at regular intervals of time. The progress of the reaction was monitored by the disappearance of 400 nm peak with a simultaneous appearance of a new peak at 300 nm.

6B.2.9. Study of antibacterial activity of the nanocomposite

Antibacterial tests of the nanocomposites were done by well diffusion method as reported in literature [47] using *Staphylococcus aureus* (MTCC 3160) and *Bacillus subtilis* (MTCC 121) as gram-positive, and *Klebsiella pneumoniae* (MTCC 618) and *Pseudomonas aeruginosa* (MTCC 1688) as gram-negative bacterial strains. An amount of 200 µL of a log phase culture of the test microbes was seeded on the surface of the Muller Hinton agar on Petri dishes. The nanocomposites were dispersed in sterilized water by ultrasonication for 10 min and 100 µL of each put into the individual wells (diameter 6 mm). The zone of inhibition diameters was measured using a transparent ruler after incubating for 24 h at 37 °C. For growth curve analysis of the microbes, the cultures were taken in conical flasks. An amount of 200 µL of the samples was added to the corresponding conical flasks and incubated for 24 h at 37 °C. One conical flask without sample was taken as the control for each microbe. In this case, gentamicin was used as the positive control for measurement of antibacterial activity. The growth of the microbes was measured by checking optical density (OD) at 620 nm after every 2 h and the OD was taken up to 25 h.

6B.2.10. Separation of crude oil and water from their mixture

A thin film of PCTN2.5 was cast on the surface of a normal filter paper and heated at 100 °C for 4 h in an oven. The thickness of the film was 0.16 mm. Then it was used for separating crude oil and water from their mixture using a suction filtering system. Here it is pertinent to mention that the crude oil obtained directly from oil pool was heated with water at 70-75 °C for about 30 min and then this liquid mixture was filtered in a suction pump using the above coated membrane. The original filter paper was also used for the same purpose to find the difference.

The efficiency of oil/water separation was defined as oil rejection coefficient R (%) and calculated according to the following equation [48].

$$R\ (\%) = M_s/M_o \quad \text{.....(Eq. 6B.1)}$$

where M_s and M_o are masses of initial water and collected water respectively.

UV-vis analysis was carried out to analyze the filtrate from where oil rejection value is calculated by using the following formula [49].

$$R\ (\%) = (1- C_0/C) \quad \text{.....(Eq. 6B.2)}$$

where C_o and C are the concentration of feed and the filtrate respectively.

Further, water flux of the separable membrane was calculated using the following equation [48].

Flux = V/S.t .....(**Eq. 6B.3**)

where V is the volume of water that permeates through the fabricated membrane, S is the effective area of the fabricated fabric and t is the time for complete separation.

6B.3. Results and Discussion

6B.3.1. Fabrication of the nanocomposite

The nanocomposite of WHPE and water dispersible CD@TiO_2 nanohybrid was fabricated through a simple *in-situ* polymerization technique. Both the polyester and the nanohybrid are environmentally friendly as well as fabrication process enjoys the advantages of waterborne system. In addition, most of the precursors used for fabrication of polyester and nanohybrid are naturally renewable i.e., bio-based; where the amount of bio-based raw materials is 56.27% in polyester and 44% in the nanohybrid. Furthermore, the nanocomposite was obtained through a greener approach in the absence of solvent, catalyst and neutralizing agents and a facile environmentally benign hydrothermal method was used for the preparation of nanohybrid. Some raw materials of HBGE and PAA are also bio-based. Thus, the approach is in accordance with some of the principles of Green Chemistry. In addition, the pristine WHPE is a biodegradable material as observed in **sub-Chapter 2B**. Thus, from the material as well as processing point of views, the nanocomposite has considerable greener contribution.

During the fabrication process the different oxygeneous functional groups of the nanohybrid interact covalently or non-covalently with the functional groups of polyester matrix, as shown in **Scheme 6B.1**. These types of interactions not only help in uniform dispersion of the nanohybrid in the polyester matrix but they also generate significant amount of interfacial domain. This is responsible for improvement in performance of the resultant material. Further, the presence of large numbers of polar functionalities in the nanocomposites helps in formation of stable dispersion in most of the organic solvents like DMF, DMSO, DMAc, ethanol, acetone, THF, methanol, etc.

6B.3.2. Characterization of the nanocomposite

The presence of functional groups in the nanocomposites was confirmed from FTIR spectral (**Figure 6B.1a and 6B.1b**) studies.

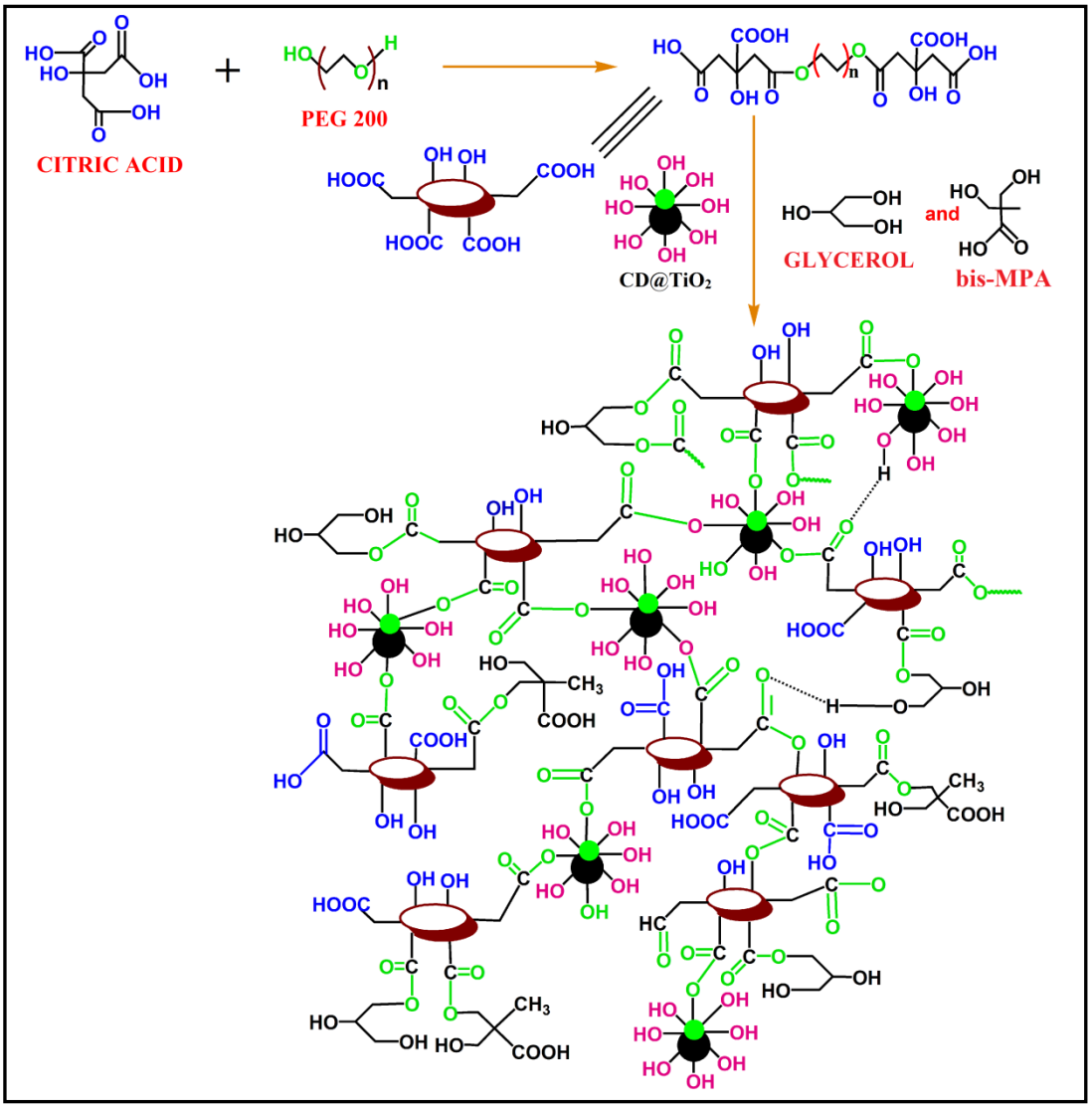

Scheme 6B.1: Proposed scheme for fabrication of WHPE/CD@TiO_2 nanocomposite

From the FTIR spectrum of bare TiO_2 (**Figure 6B.1a**), -O-H stretching and bending bands were observed at 3434 and 1632 cm^{-1} respectively [50].The broad band observed at around 681 cm^{-1} is assigned to the stretching mode of Ti-O bond, while the band at 1400 cm^{-1} is arising from TiO_2 lattice vibrations [36]. The stretching and bending -O-H absorption bands of TiO_2 are shifted due to the formation of the nanohybrid. Further, the additional absorption bands at 2922 cm^{-1} and 2852 cm^{-1} are assigned to -C-H asymmetric and symmetric stretching vibrations in the nanohybrid. However, the band at 681 cm^{-1} gets shifted to ~606 cm^{-1} after formation of nanocomposite [51]. Marginal shifts of some other FTIR absorption bands of polyester were also observed. The shifting of the bands indicates the interactions of carboxylic and hydroxyl groups of polyester matrix with the nanohybrid through hydrogen bonding or other polar-polar interactions. Further, the

broad band at 3500 cm^{-1} is attributed to hydroxyl groups of nanohybrid and polyester matrix.

XRD pattern of pristine polyester (**Figure 6B.1c**) showed a single board peak in the range of 10-30° indicating its amorphous nature. In XRD patterns of the nanocomposites (**Figure 6B.1d**), it is seen that the intensity of original peaks of the nanohybrid as well as pristine system decreased and the peaks were broadened. Further, some of the peaks for the nanohybrid in the nanocomposite were diminished due to the presence of low amount of nanohybrid in the nanocomposite as well as interactions between polyester matrix and nanohybrid. These results indicate the structural modification of both the nanomaterial and polyester [31, 32].

The surface morphology of the nanocomposite and the state of dispersion of the nanohybrid in the polyester matrix were studied from TEM analyses. A good dispersion of the nanohybrid in the matrix is crucial to achieve the desired nano-reinforcing effect and thereby obtaining a high performing material.

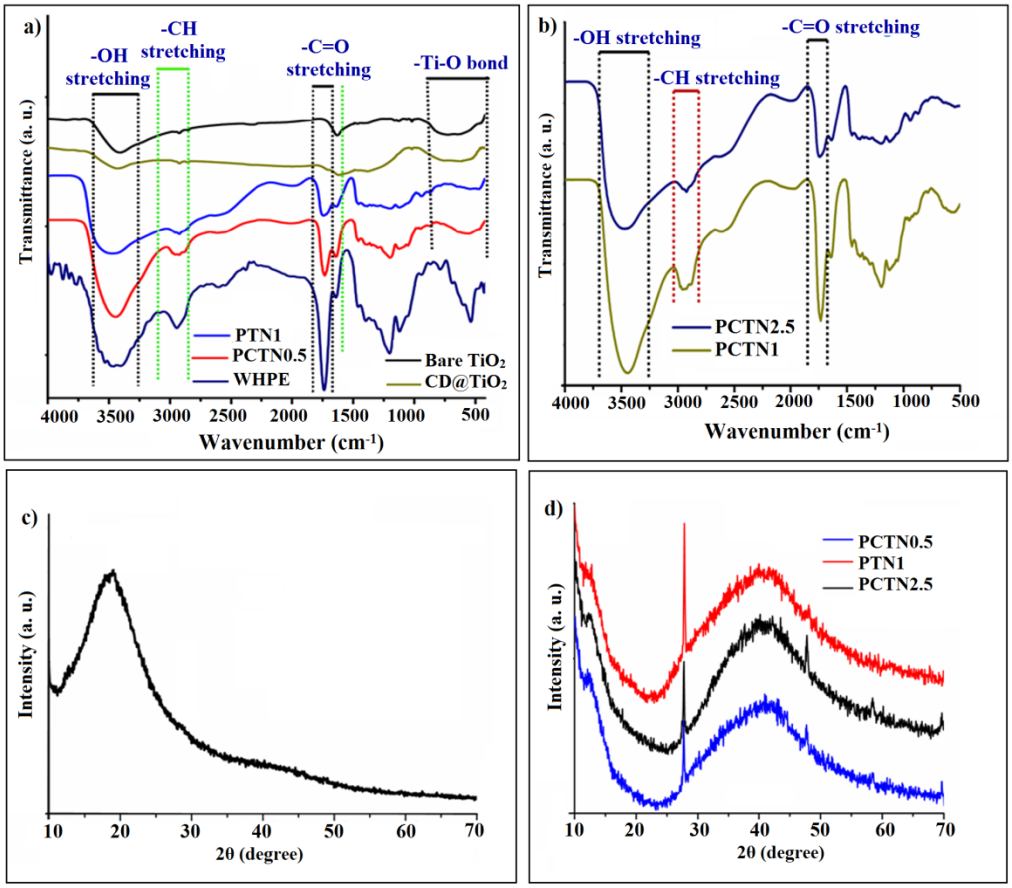

Figure 6B.1: (a, b) FTIR spectra of the nanohybrid and the nanocomposites, and XRD patterns of **(c)** WHPE and **(d)** the nanocomposites

The representative TEM images of PCTN2.5 displayed the homogeneous distribution of the nanohybrid in the polyester matrix as shown in **Figure 6B.2 (a-c)**. The crystal lattice fringes with a d-spacing of 0.36 nm correspond to the (101) plane of anatase TiO_2 [47] and the lattice spacing of 0.32 nm corresponding to (002) plane of CD [47], were also observed in HRTEM images (**Figure 6B.2d and 6B.2e**). Further, the selected area electron diffraction (SAED) pattern (**Figure 6B.2f**) of the nanocomposite reveals semi-crystalline nature of the nanocomposite which may arise due to the crystallinity of TiO_2 nanoparticles.

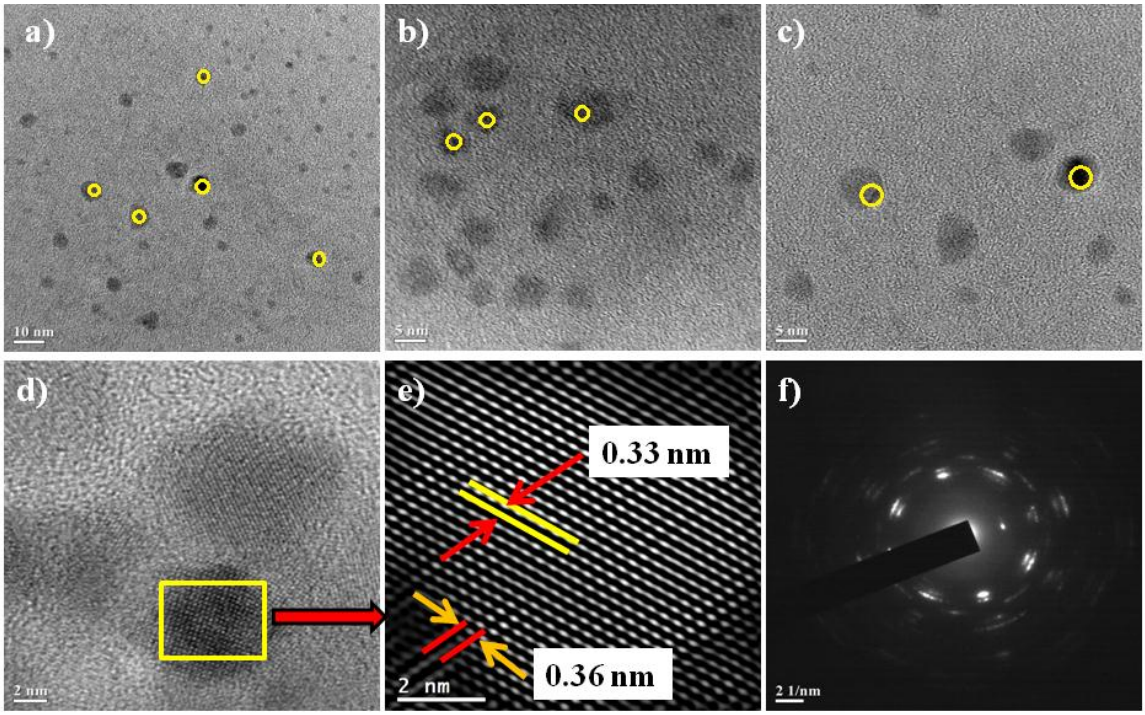

Figure 6B.2: (a-c) TEM images of PCTN2.5 at different magnifications, **(d, e)** lattice fringes and **(f)** SAED pattern

6B.3.3. Rheological study of the nanocomposites

Rheological study of the nanocomposite was carried out with the help of a rheometer to achieve some information about the interactions between the nanohybrid and the polyester matrix [51]. The variations of shear viscosity against time and temperature under controlled stress and a single shear value were examined for all the nanocomposites before curing. The results are shown in **Figure 6B.3a and 6B.3b**. It is noticed that the viscosity remained almost constant with time. The nanocomposites exhibited higher viscosity than the pristine polyester due to the presence of interfacial

interactions between the rigid nanomaterials with the flexible polyester matrix. Furthermore, dose dependent viscosity was also obtained for the nanocomposites. However, the shear viscosity of all the nanocomposites decreased with the increase of temperature. This is due to the increase in kinetic energy of the different components present in the nanocomposites, which decreases the structure forming tendency of the polymer molecules and thus resulted decrease in viscosity. Further, viscoelasticity is a combination of elastic (solid-like) and viscous (liquid-like) behaviors, and are usually described by storage modulus (G′) and loss modulus (G″) respectively [52]. These parameters were measured as a function of frequency (1-10 s^{-1}) under constant temperature (25 °C) and constant stress (20 Pa). The dependence of the viscoelastic behavior of nanocomposite on the loadings of the nanohybrid was also studied. The results are shown in **Figure 6B.3c and 6B.3d** and it is noticed that both G′ and G″ increase with the increase of frequency (1-10 s^{-1}) at different rates as well as with the loadings of the nanohybrid. The trend of changes was in good agreement with the results demonstrated in the literature [52, 53]. This is due to the improvement of elastic behavior of the nanocomposites upon incorporation of the nanohybrid. This improvement arises from the strong interactions between nanohybrid and the polymer matrix. The solid-like elastic behavior, i.e., G″<G′ of the nanocomposites is due to combination of polymer-nanohybrid and polymer-polymer interactions. This indicates the formation of a continuous network inside the polymer matrix. Furthermore, the variation of G′ and G″ with respect to temperature (from 25 to 75 °C) under constant frequency (1 Hz) and controlled oscillatory stress of 20 Pa are also shown **Figure 6B.3e and 6B.3f**. The decrease in G′ and G″ values with the increase in temperature was observed for all the nanocomposites. This is owing to the increase in kinetic energy and free volume of the polymer chains, which in turn decreases inter- and intra-molecular interactions as well as entanglement density in the system. Thus, this result clearly demonstrated strong interactions between nanohybrid and the polyester matrix [51-53].

6B.3.4. Curing of the nanocomposite

The nanocomposite was cured with HBGE and PAA through cross-linking reactions of different reactive functional groups such as -OH, -COOH, $-NH_2$ and epoxide present in the system. A large number of polar-polar, hydrogen bonding, etc. interactions are also occurring during this curing process. All such plausible interactions and chemical reactions are shown in **Scheme 6B.2.**

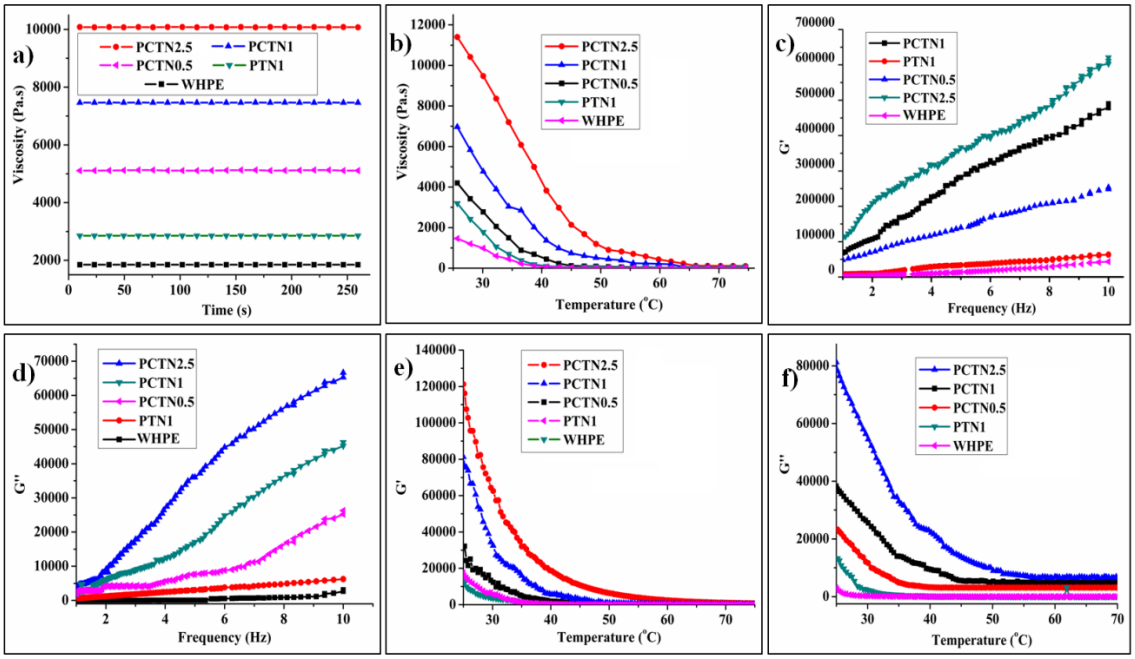

Figure 6B.3: Rheological behavior of the nanocomposites. Variations of shear viscosity against **(a)** time and **(b)** temperature under constant stress, and variations of **(c)** G′ and **(d)** G″ with frequency and variations of **(e)** G′ and **(f)** G″ with temperature

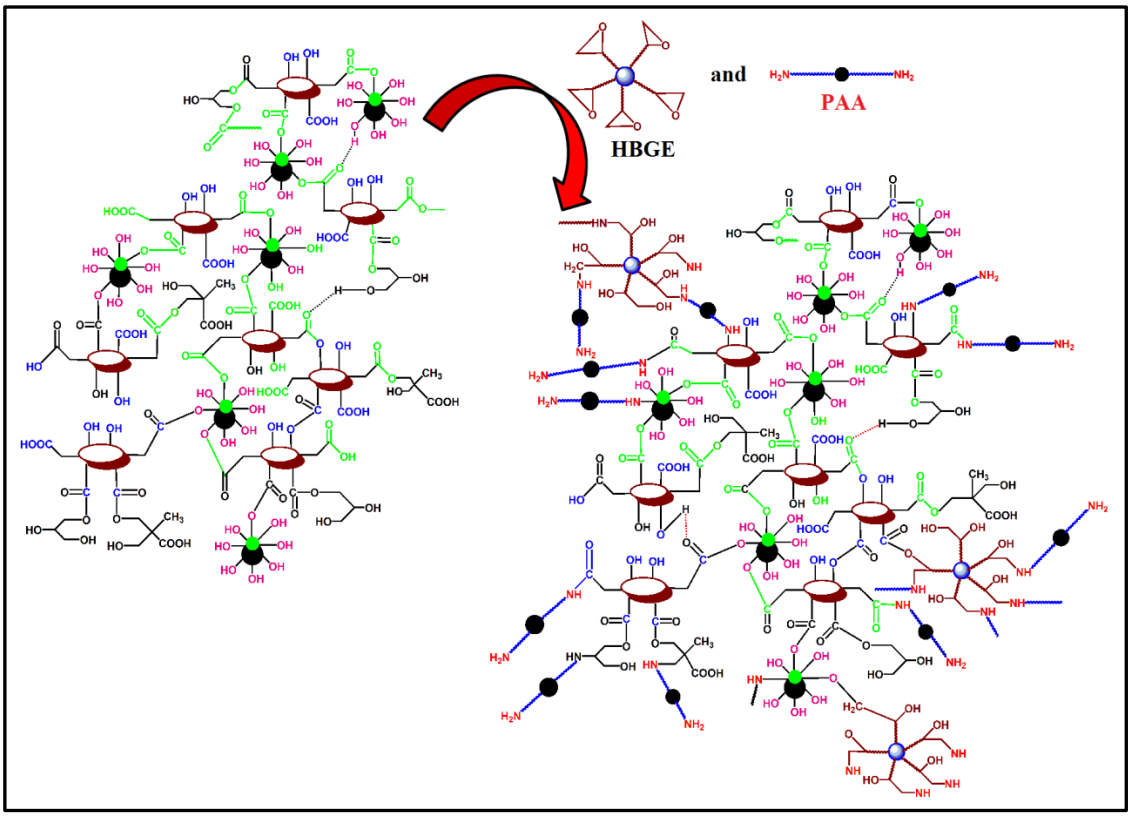

Scheme 6B.2: The plausible cross-linking reactions occurred during formation of the thermosetting nanocomposite

The $–NH_2$ groups of hardener, and free -OH group of polyester and nanohybrid were interacted with the epoxide groups of HBGE. The transesterification reaction between -OH and -O-C=O groups may also occur. Further, hydrogen bonding was formed between -C=O of the nanocomposite and -OH of both HBGE and nanohybrid. The hydroxyl-epoxy etherification reaction also occurred [54]. The rate of curing of the nanocomposites was found to be higher than the pristine system. This is due to the increase in the number of such functional groups with increase in loading of nanohybrid (**Table 6B.1**).

6B.3.5. Performance characteristics of the nanocomposites

The improvement of mechanical properties of the nanocomposites is the central interest in fabrication of such materials. The nature of branching in the polymer chain plays a significant role in contribution of mechanical properties and increase in amount of polar side chains in polymer backbone results in an enhanced tensile strength. Further, functional groups of nanocomposite play a vital role in increasing the interaction energy between nanomaterial and polymer matrix [52]. The interaction between the nanohybrid and matrix is significant because of uniformly dispersed nanoparticles in a polymeric matrix impart a high portion of interface owing to their high surface area. The weak interactions between them result lower mechanical strength than the pristine system as the external applied load of the nanocomposite is unable to transfer to the nanomaterials [54-56]. The mechanical properties such as tensile strength, toughness, elongation at break, impact resistance, Young's modulus and scratch hardness values of the nanocomposites were evaluated and the results are given in **Table 6B.1**. It is seen that the incorporation of even a small amount of the nanohybrid significantly improved the performance of the pristine polyester. This may be due to the combined effect of small size, large surface area and quantum confinement of the nanohybrid as well as strong interfacial interactions of it with the polyester matrix [56, 57]. The tensile strength of pristine polyester was improved after the formation of nanocomposite with both bare TiO_2 and CD@TiO_2 nanohybrid, however the nanocomposite with 1 wt% bare TiO_2 showed lower value of tensile strength than the nanocomposite with nanohybrid (1wt%). This is due to incompatibility, aggregation and absence of suitable functionality of TiO_2. However, in case of nanohybrid, CD helps in better dispersion and stabilization of it due to the presence of large number of polar functional groups which can interact with the polyester matrix.

Table 6B.1: Performance characteristics of WHPE and the nanocomposites

Property	**WHPE**	**PTN1**	**PCTN0.5**	**PCTN1**	**PCTN2.5**
Swelling value (%)	22 ± 2	23 ± 2	2 ± 1	22 ± 1	21 ± 1
Curing time (h)	5 ± 0.25	4 ± 0.25	3 ± 0.25	2.5 ± 0.5	1.5 ± 0.5
Tensile strength (MPa)	7.8 ± 2.3	15 ± 3	27 ± 2.8	33.5 ± 2	52 ± 3.5
Elongation (%)	245 ± 8	142 ± 10	221 ± 5	215 ± 4	182 ± 5
Scratch hardness (kg)[a]	4 ± 1	7 ± 0.5	9 ± 1	>10	>10
Impact resistance (kJ m^{-1})*	>8.3	>8.3	>8.3	>8.3	>8.3
Toughness (MJ m^{-3})[b]	17.2 ± 3.5	18.1 ± 2.8	30 ± 3.2	56.2 ± 4	65.5 ± 3.5
Gloss (°)	80 ± 2	85 ± 1	90 ± 3	98 ± 2	105 ± 2
Young's modulus (MPa)	243 ± 3	270 ± 2	309 ± 2	350 ± 3	420 ± 2

*[a,]*Highest limit of the instrument and [b]calculated from area under stress-strain curves*

Further, the mechanical properties of the nanocomposites were found to be highly dependent on the loading of the nanohybrid. As the loading of nanohybrid increases, the mechanical strength of the nanocomposite was also improved in the same manner. The tensile strength of PCTN2.5 increases 6.6 times than the pristine polyester. The nanoscale size effect of nanohybrid can lead to a close association with the polyester matrix which may be strengthened with the increase of nanohybrid loading. This tensile strength value is found to be superior to the reported polyester/MWCNT (28-35 MPa) [55], vinyl ester/TiO_2 (3.70 to 5.72 MPa) [56], polyester/clay (2.42-6.28 MPa) [58], polyester/CD (26.1 MPa) [59], polyethylene/TiO_2 (11.3-12.7 MPa) [57], poly(ethylene terephthalate)/TiO_2 (27.1-34.4 MPa) [60], polyurethane/TiO_2 (6-8 MPa) [61] and blended epoxy/polyester/clay (20-29.7 MPa) [62] nanocomposites. However, values of elongation at break decreased after formation of nanocomposite and also decreased with increase in the loading of nanohybrid. Even then the strain value (>200%) of the

nanocomposites was significantly high. This is because of the presence of different flexible moieties like aliphatic moieties of polyester and hardener, ether linkages, etc. as well as plasticizing effect of the long hydrocarbon chain of hardener [59]. Further, the interactions shown in **Scheme 6B.2** are associated with various secondary interactions such as polar-polar interaction, hydrogen bonding, etc. of the polar functional groups, which may help in full molecular chain extension of the polyester. Furthermore, graphitic structure of CD with polar functional groups may result good flexibility due to slippage of layers during application of high load. The polar functional groups of CD also provide strong physico-chemical interactions with the polar groups of polyester, HBGE and PAA hardener and help in extension of chain length. Further, these values are found to be better than the already reported nanocomposites of epoxy/TiO_2 (2-3.5 %) [1], polyester/ clay (12.45%) [58], PET/clay (2-3%) [55] polyester/MWCNT (4-8%) [54], polylactide/TiO_2 (10.4-19.1%) [63], PET/TiO_2 (30.5-34.4%) [60] and polyester/CD (162%) [59]. Typical stress-strain curves and tensile process of the nanocomposites are shown in **Figure 6B.4** and areas under these curves were used to measure toughness of the material. The toughness of the nanocomposite was also found to be enhanced and the values were increased with the loading of the nanohybrid. The values were superior to reported polyester/CD (32.8 MJ m^{-3}) [59] and poly(phenyl sulfone)/TiO_2 nanocomposite (15.5-20 MJ m^{-3}) [64]. Further, the toughness of the thermoset was drastically enhanced the other mechanical properties such as impact resistance and scratch hardness. So these properties were also improved after formation of nanocomposites. The impact resistance was higher than the epoxy blended polyester/TiO_2 nanocomposite (4.6-5 J m^{-1}) [62] and 1-7 wt% TiO_2-based unsaturated polyester nanocomposite (4.2-6 kJ m^{-1}) [65]. The enhancement of these properties is ascribed to the significant interfacial interactions and good compatibility between polyester matrix and the nanohybrid. The fine sizes of CD and TiO_2 provide a large surface area for strong interactions with the matrix, and thus all the mechanical properties of the nanocomposites were improved without much affecting the flexibility. The peripheral polar functional groups of the nanohybrid also provide strong physico-chemical interactions with HBGE and PAA; which also help in enhancement of mechanical properties of the nanocomposites [1, 3, 54-56]. Further, Young's modulus value of the nanocomposite was also increased dramatically with the loading of nanohybrid and this may happen due to favorable size and distribution of the nanohybrid that cause strong interactions between the nanohybrid and polyester matrix.

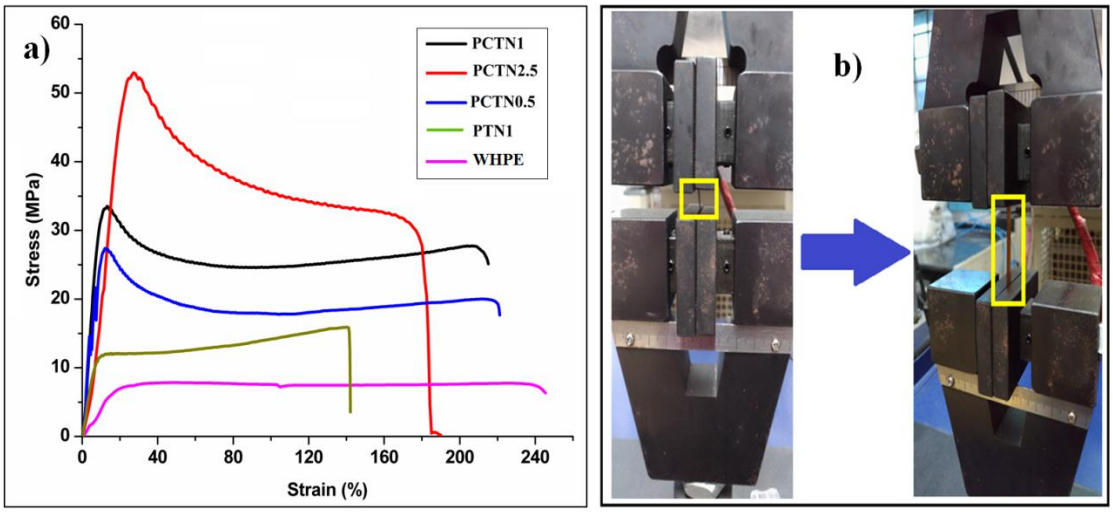

Figure 6B.4: (a) Stress-strain profiles of the nanocomposites and **(b)** image of tensile test showing >200 strain

Again the elastic components of the material are in turn related with the bare polymer matrix, nanomaterials and their cross effect. The nanomaterial contains some polar functional groups and interfacial interactions with the polyester matrix are higher with higher loading of nanomaterial. Thus the chain stiffening increases with the increase of nanomaterials loading due to proportionate increase of interfacial interactions between the flexible polymer chains and rigid nanohybrid. These interactions arise from different secondary interactions like polar-polar interaction, hydrogen bonding, etc. as well as covalent bond formation. Thus, as PCTN2.5 and PCTN1 contain higher amount of nanomaterials compared to the others and showed higher value than others.

6B.3.6. Thermal properties of the nanocomposites

The thermal stability of the nanocomposites was studied from thermogravimetric analyses. The initial degradation temperature of polyester thermosets increased after formation of nanocomposites with bare TiO_2 as well as CD@TiO_2 nanohybrid. The initial degradation temperature further increased with the increase of amount of nanohybrid loading (**Figure 6B.5a**). The improvement in thermal stability is due to high cross-link density, strong covalent and non-covalent interactions along with some secondary interactions like polar-polar interactions and hydrogen bonding, etc. [54]. Both the pristine thermoset and the nanocomposites were degraded mainly through two stage degradation patterns as observed in TG curves, where the first step (250-270 °C) is related to the degradation of thermolabile aliphatic moieties, whereas the second stage

(330-350 °C) is due to degradation of thermostable aromatic moieties. However, DSC results (**Figure 6B.5b**) clearly revealed no significant difference in T_g values between the pristine polyester and nanocomposite due to contradictory effect of increasing intermolecular attractive forces as well as the occurrence of PEG shell around the nanohybrid. This interaction of flexible PEG chain is due to favorable compatibility of the nanohybrid containing Ti-O bonds with the -O- linkages of PEG [66].

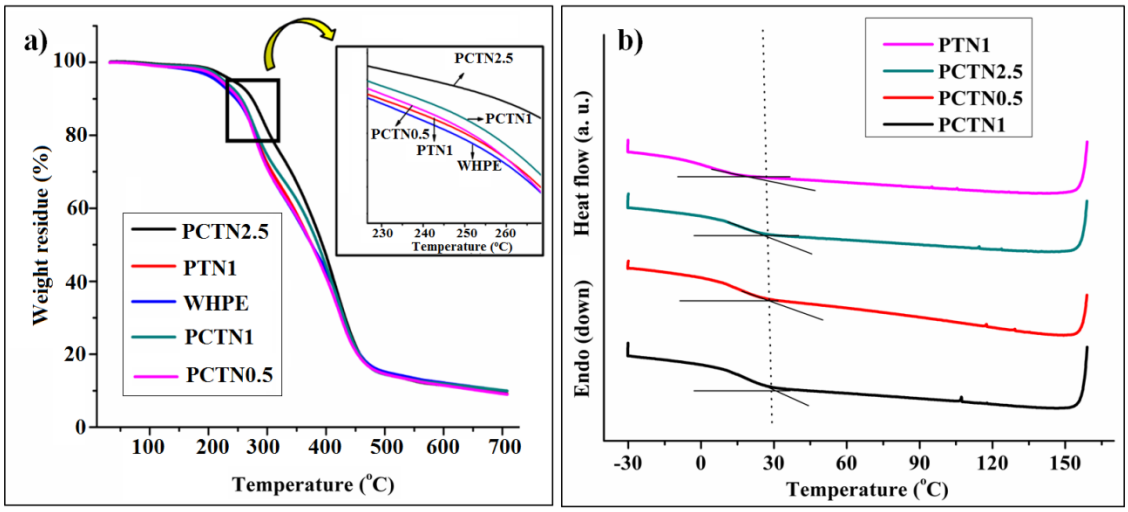

Figure 6B.5: (a) TG thermograms and **(b)** DSC curves of the nanocomposites

6B.3.7. Optical properties

The optical properties of the nanocomposites were studied by using UV-vis and PL spectroscopic techniques. In the UV-vis spectrum of bare TiO_2 no absorption in the visible region (400-800 nm) was observed as already described **sub-chapter 6A**, while both the nanohybrid (**Figure 6A.7**, in the previous sub-chapter) and nanocomposites (**Figure 6B.6a**) showed a noticeable absorption in this area. In brief, it is evident that introducing CD can enhance the visible light photocatalytic activity of both the nanohybrid and the nanocomposites. Hence, the key role of uniformly distributed CD on the surface of TiO_2 is to absorb light in the visible region which can convert light from higher wavelength to shorter wavelength and thereby increasing the light absorption efficiency of the nanohybrid [47]. Further, the optical colors of the nanocomposites both before and after curing in the visible light, at shorter UV (254 nm) as well as longer UV (365 nm) region are shown in **Figure 6B.6b** and **6B.6c**. The color of both polyester nanocomposite and cured film was brown under visible light. This brown color changed to green on exposure of long UV light and to dark blue under short UV light. The color

change at different wavelengths of UV light is due to the presence of different sizes of nanohybrid in the nanocomposites.

Further, the optical band gap was determined from the intercept of tangent with the *x*-axis, using $(\alpha h\nu)^{1/2}$ *vs* energy plots ($h\nu$) as shown in **Figure 6B.6(d-f)**. Bare TiO_2 showed a band-gap of around 3-3.3 eV, while CD@TiO_2 exhibits reduced band-gap onset energy of 2.8 eV due to the additional electronic state above the valence band of TiO_2 and its visible absorption was extended down to 1.5 eV, leading to conjecture the visible light active photocatalysis of the developed systems [47]. This reduction in band gap is due to the interfacial interaction. Thus a more efficient utilization of light could be obtained because of this to increase the light absorbance [67].

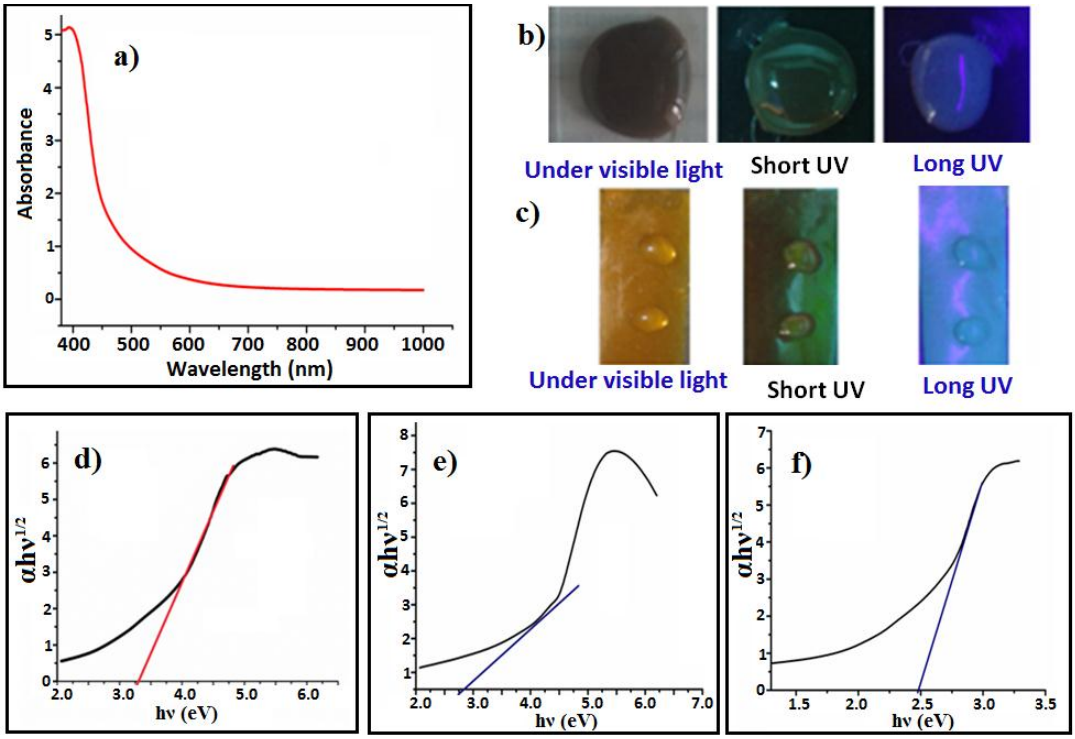

Figure 6B.6: (a) UV-vis spectrum of PCTN1, **(b, c)** emission of different colors under visible, short and long UV light by the nanocomposite; and band gaps of **(c)** TiO_2, **(d)** CD@TiO_2 and **(e)** PCTN2.5

In addition, the nanocomposite can also be used in the security ink as it has the unique properties like non visibility under visible light but provides different colors at different wavelengths of UV light. In addition it also exhibited excellent thermal and photo stability, good compatibility with other materials, etc. For this purpose a solution of nanocomposite at concentration of 2 mg mL^{-1} was used to write the structure of

phenol on a filter paper which was not visible under visible light. However, the same can be clearly seen under the illumination of a 365 nm UV light (**Figure 6B.7a** and **6B.7b**). This information can be seen repeatedly as and when required under exposure of such wavelength of light. Thus, this nanocomposite based security ink can be used for preserving and secretly communicating important information particularly for defense system.

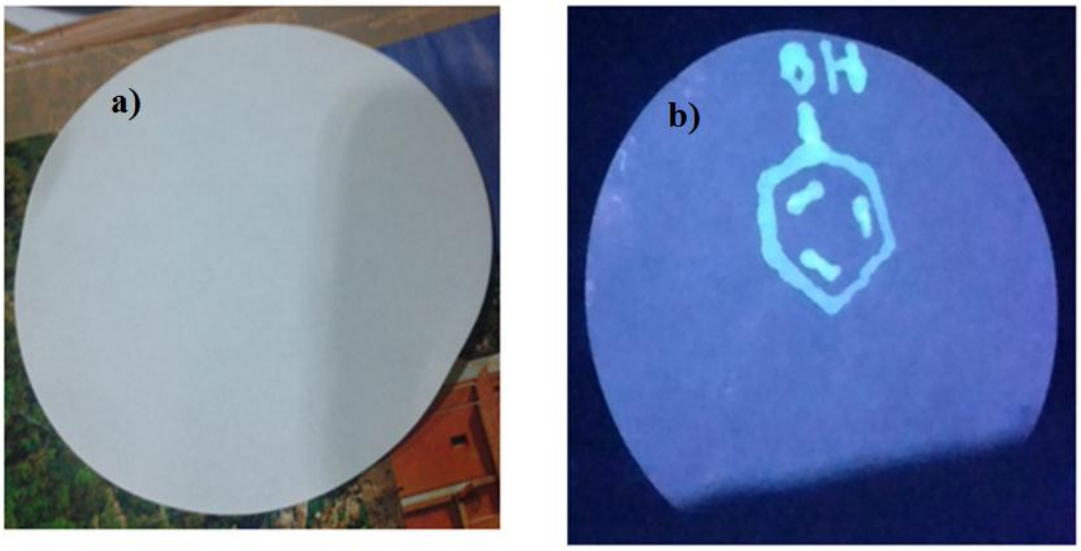

Figure 6B.7: Coated filter paper under **(a)** visible light and **(b)** UV light (365 nm)

PL properties of the nanocomposites were also evaluated with the help of a PL spectroscopy. PL was used to confirm the up-conversion property as well as separation efficiency of a photogenerated e^-/h^+ pairs. CD possesses excellent up-conversion property with an emission maximum at 350 nm (λ_{ex} = 700 nm) (**Figure 6B.8**), which can excite the valence electrons in TiO_2 to generate an e^-/h^+ pairs. The nanohybrid upon excitation in the visible region also showed an emission maximum in the UV region. Therefore, after incorporation of this nanohybrid into polyester matrix, the nanocomposite exhibited both wavelength dependent down- and up-conversion PL properties. Upon excitation from 340 to 420 nm, they showed corresponding emission spectra in the region of 440-510 nm (**Figure 6B.8**) and confirmed the wavelength dependent down-conversion property. While, upon exciting nanohybrid in the wavelengths from 700 to 800 nm corresponding emission spectra were appeared from 440 to 520 nm (**Figure 6B.8**) which confirmed the wavelength dependent up-conversion property. This feature may be ascribed to the different emissive sites and distribution of

different particle sizes of nanohybrid as well as to active multiphoton processes [42, 43, 47].

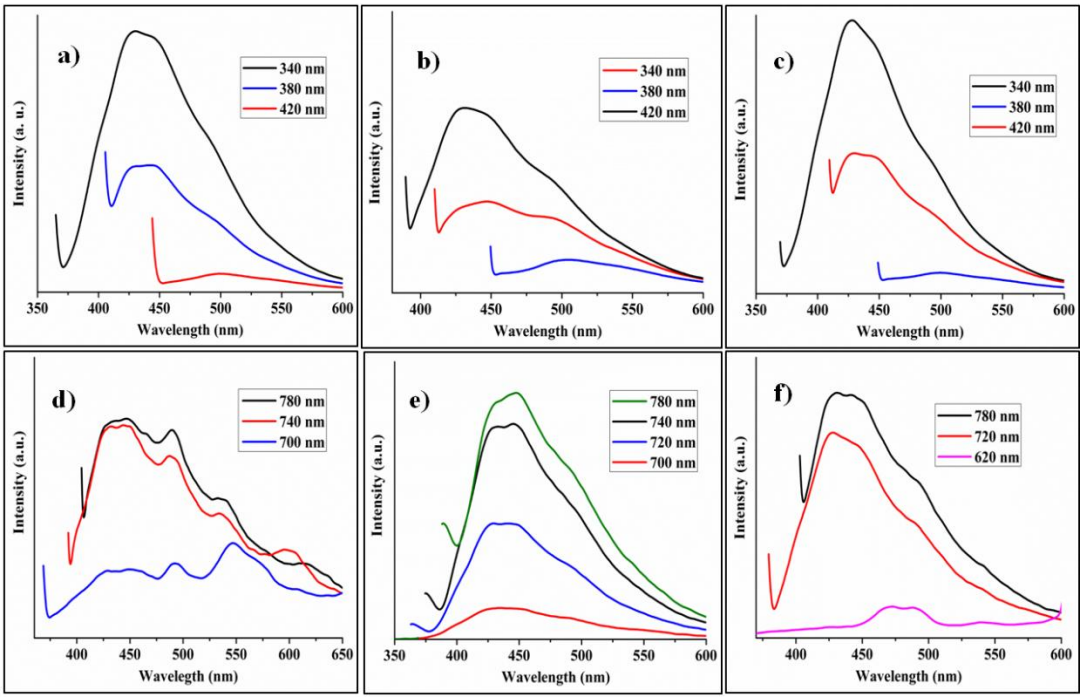

Figure 6B.8: PL characteristics of the nanocomposites: Wavelength dependent down-conversion PL spectra of **(a)** PCTN1, **(b)** PCTN0.5 and **(c)** PCTN2.5; and wavelength dependent up-conversion PL spectra of **(d)** PCTN1, **(e)** PCTN0.5 and **(f)** PCTN2.5

6B.3.8. Anti-reflecting property

The most attractive and interesting attributes of the developed nanocomposites systems were their ability to show anti-reflecting property. These properties are commonly studied for polymeric materials with TiO_2 where compatibility poses a question. In this milieu, CD with polar functional groups not only helps to stabilize TiO_2 nanoparticles but also significantly improves compatibility with organic polymer, as supported by spectral analysis [41]. The anti-reflectance property of the nanocomposite was obtained from the transmittance value as measured by UV-vis spectral study (**Figure 6B.9**). From this figure, it is seen that the light percentage transmittance (T%) of the nanocomposites coated glass slides is higher than uncoated glass slide. This enhancement of light transmission is due to the anti-reflecting properties of the nanocomposite films, contributing to the decrease of the effective refractive index of the films. Further, the nanocomposite films are still transparent and the retention of high transparency of them is because of small particle size and the uniform film morphology without pores and

aggregates [48]. The film of PCTN0.5 showed the highest transmittance of 96.2% at a wavelength of 800 nm. The transmittance other nanocomposite films lies in the range of 88.9-91.2% (600-1000 nm). It is possible to monitor that all the nanocomposites showed an enhancement in transmittance compared to pure TiO_2 based polymeric film (polyester/TiO_2). This can be described by the fact that TiO_2 has higher refractive index (n≈2.5) than the nanohybrid and therefore, resulted in lower %T of the films. While %T of the nanocomposite films decrease with increase in the loadings of CD@TiO_2.

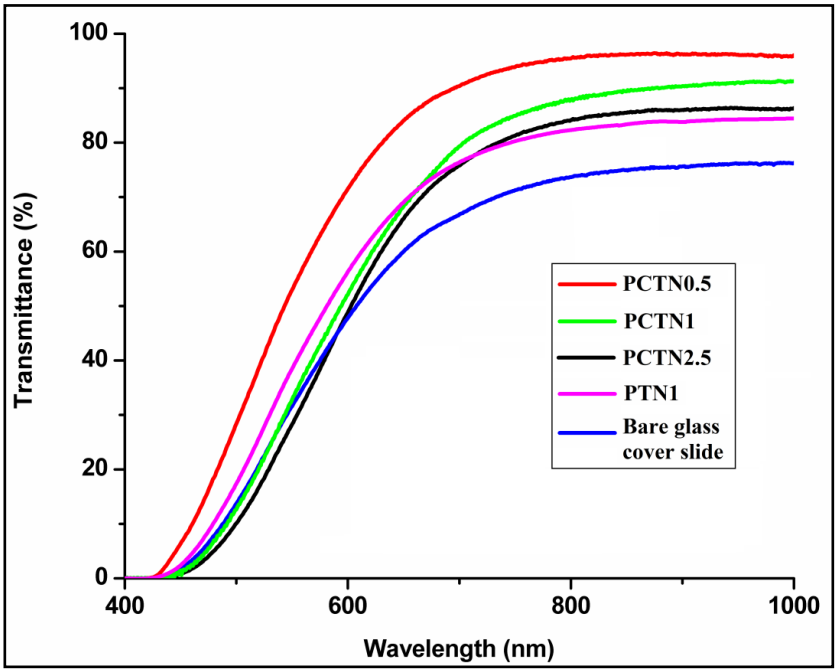

Figure 6B.9: Transmittance spectra of the nanocomposites

These transmittance values are higher than the other anti-reflecting films like GO coated glass (76%) [5], TiO_2/SiO_2 composite films (85%) [49], etc. in the visible range. The transmittance (96.2%) of PCTN0.5 was found to be superior to reported chlorotrimethyl silane and 3-mercaptopropyltrimethoxy silane modified ZnO-based polystyrene nanocomposite (91.9-89.8%) [67], 0.5 vol% TiO_2 based poly(ethylene terephthalate) nanocomposite (85-95%) [50] and polylactide/TiO_2 nanocomposite (71.6-93.1%) [68]. Further, the glass coated polymer nanocomposite with 90 wt% dispersed fumed silica showed transmittance of 88% [52], which are also inferior to the fabricated nanocomposite. It is noticed from the reported literature that the fabricated polyester nanocomposite exhibited either comparable or higher transmittance than the other materials. Further, the reported method used functionalizing agent as well as other

preparative method and organic solvent for dispersion of nanomaterials. Furthermore, compared to these metal based materials, polymeric materials used as substrate have many advantages such as low cost, good flexibility, good adiabatic performance, etc. Thus, the nanocomposite acts as an excellent anti-reflective surface which can be used in different optical technologies for reducing the reflectivity at the interfaces.

6B.3.9. Anti-fogging and anti-icing attributes of the nanocomposites

Prevention of fog is a daunting challenge for various optical applications of transparent materials. This is due to the reason that fog reduces the effectiveness of light transmission and hence the optical efficiency [7, 9-11]. The anti-fogging property of the nanocomposite was checked by placing the sample inside a refrigerator for minimum 30 min and then exposed to a humid laboratory environment. The visual transparency of both the bare glass and nanocomposite films are shown in **Figure 6B.10 (a-c)**. From this figure, it is seen that the bare glass slide after taking out from refrigerator under ambient conditions fogged immediately and presented a large amount of tiny condensed droplets causing a significant reduction of the optical transmittance and the words below are blurred. While the nanocomposite film (PCTN2.5) significantly prevent the formation of fog and exhibited excellent transparency, and the words written below the film were clearly visible. Thus, the nanocomposite film plays an active role in anti-fogging property of glass. Further, the same test was performed in different samples under different humid conditions (60-80%) including boiled water and results of these are shown in **Figure 6B.11**. It is seen that the nanocomposite exhibited anti-fogging behavior in the high humidity (60-80%), thus it is expected to achieve this property in low humidity too. Further, the uncoated glass over boiling water showed condensation of water droplets and it became hazy, whereas the coated glass slide remained clear after being removed from the refrigerator (**Figure 6B.11**). The anti-fogging performance is due to the fact that the more hydrophobic is the material, lower is the rate of water cooling. Further, longer times were required to form the initial fog on the hydrophobic surface, especially on superhydrophobic surface, so that the nanocomposite covered with the least water droplets and thus remained transparent in all times [61].

The superhydrophobicity behavior of the material was explained by measuring the contact angle of the surface (135-150°) using ImageJ software (**Figure 6B.12**). The anti-fogging property of polyester nanocomposite was not found in literature and hence there is no comparison.

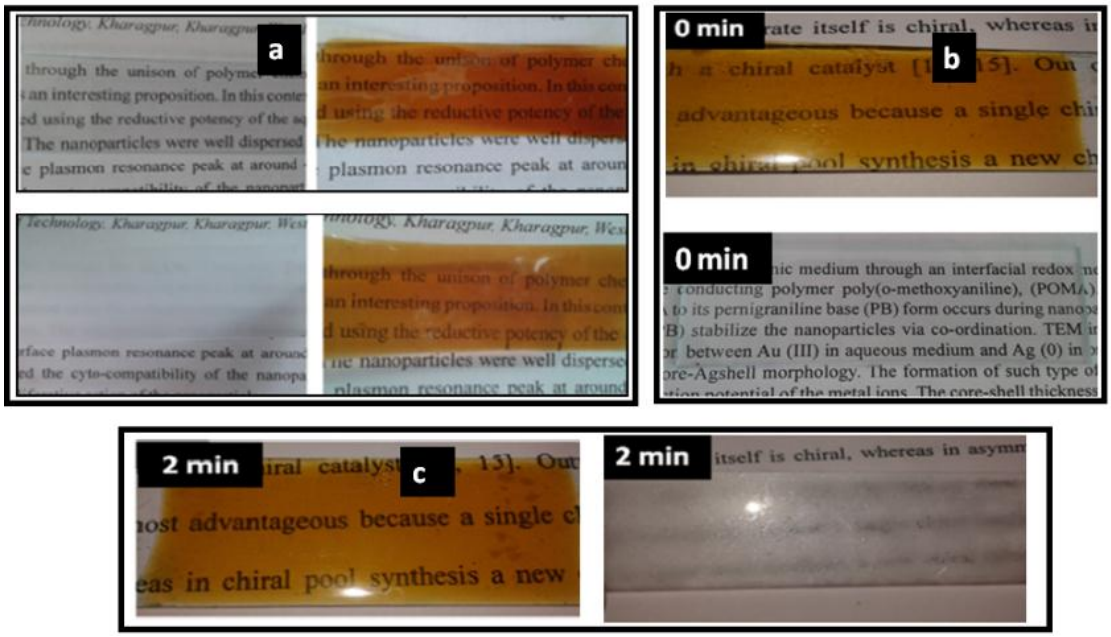

Figure 6B.10: Anti-fogging behavior of the nanocomposites. **(a)** Visual transparency of bare and coated (PCTN2.5) glass slides after super-cooling and, bare and PCTN1 coated glass slides **(b)** before anti-fogging test and **(c)** after anti-fogging test

Figure 6B.11: Photos of **(a, b)** PCTN0.5 under 70 and 76% humidity respectively; **(c)** PCTN1 and **(d)** PCTN2.5 under 76% humidity; **(e)** PCTN2.5 and **(f)** bare glass slide over boiling water after stored at -20°C

However, a few other materials are reported in literature, which include 15 wt% PEG (M_w= 1000-6000 g mol^{-1}) and 30 wt% SiO_2 modified TiO_2 films [62], PEG functionalized PVA/PAA [63], poly(vinyl alcohol)/nafion film [64], etc. with anti-fogging property.

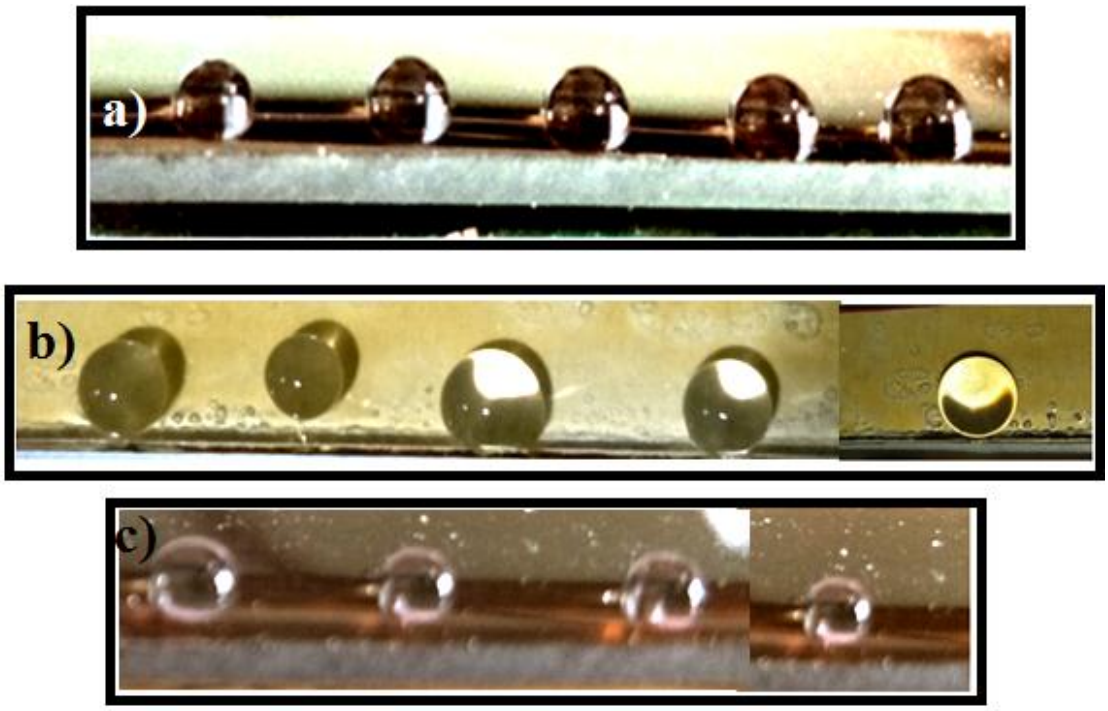

Figure 6B.12: Water droplets on **(a)** PCTN0.5, **(b)** PCTN1 and **(c, d)** PCTN2.5 surface showed the superhydrophobicity behavior

Furthermore, in recent years, to solve the adhesion and accumulation of ice; researchers were more concentrated on design of superhydrophobic surfaces with nanoparticles, nanostructures, or anti-icing coatings, as chemicals are extremely expensive, procedures are complicated and cause environmental hazard [65]. Though there are many reports on anti-icing behavior of superhydrophobic surface using nanostructure but this is the first report on anti-icing property of WHPE nanocomposite using CD@TiO_2 [66, 69, 70]. It was observed that the water droplets formed ice on both the uncoated surface of aluminum and glass substrates, whereas no ice formation was observed on the coated surface of glass and aluminum plates (**Figure 6B.13a-g**). From this figure, it is seen that after 1 min, water droplets on the uncoated surface start losing their transparency as ice formation has started, whereas the droplets on the coated surface remained transparent.

Further, the freezing delay time of water droplets on the nanocomposite surfaces was tested by placing 5 µL water droplets and keeping at -15 °C (**Figure 6B.14**) and repeated several times to get the statistical significance from ANOVA.

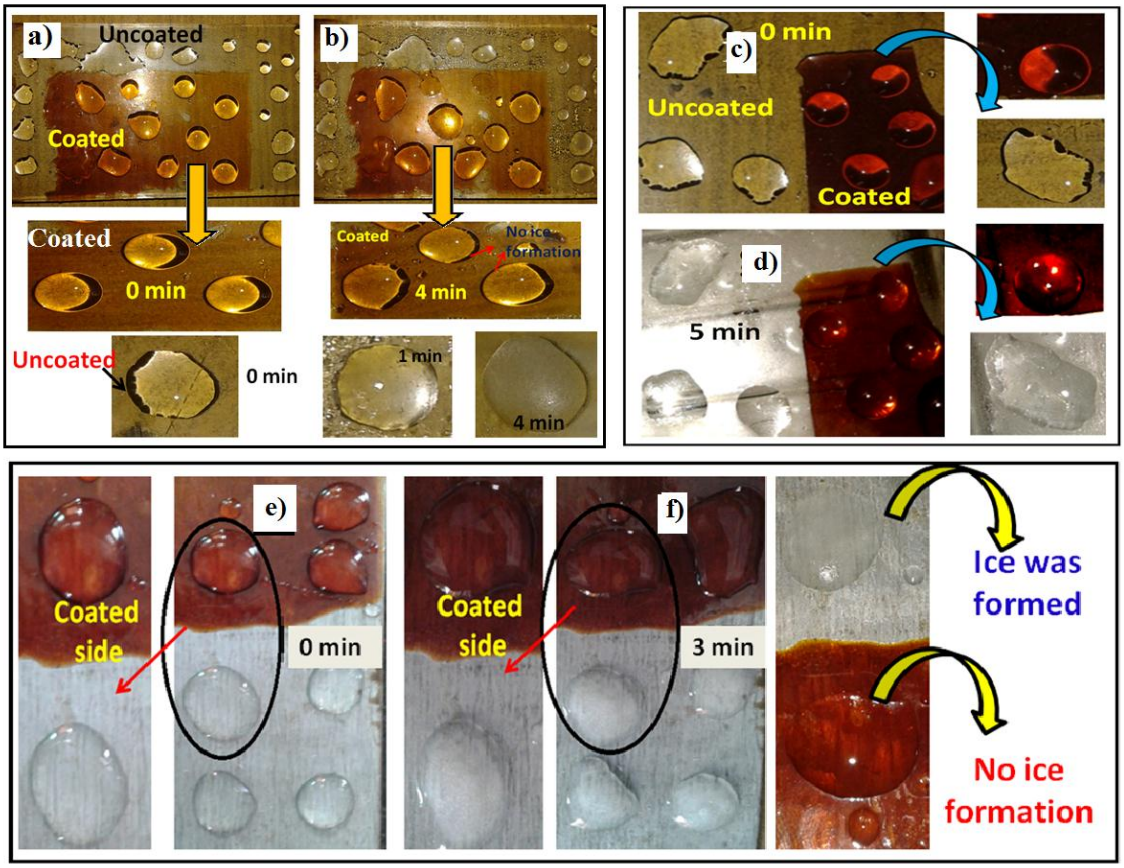

Figure 6B.13: Anti-icing behavior of the nanocomposites. Coated and uncoated glass slides with **(a, b)** PCTN0.5, **(c, d)** PCTN2.5 and **(e, f)** coated and uncoated aluminum plates with PCTN2.5

The delay time during the measuring process was defined as the time at which the water droplets began to transform from being transparent to being completely frozen. Initially, the water droplets were all transparent and the droplets with time slowly became dense, such that the light spot vanished. The freezing delay time was found to be 940s ± 40s. Furthermore, anti-icing test was performed on different surface (PCTN0.5 and PCTN1) keeping the volume of water droplet same (5µL), but shape of water droplet was found to be different (in case of bare glass slide) because of difference in their surface. It is seen from **Figure 6B.14** that all the nanocomposite showed excellent

anti-icing behavior. This is due to superhydrophobicity of the surfaces which has excellent applicants for ice-phobicity due to their extraordinary water repellency.

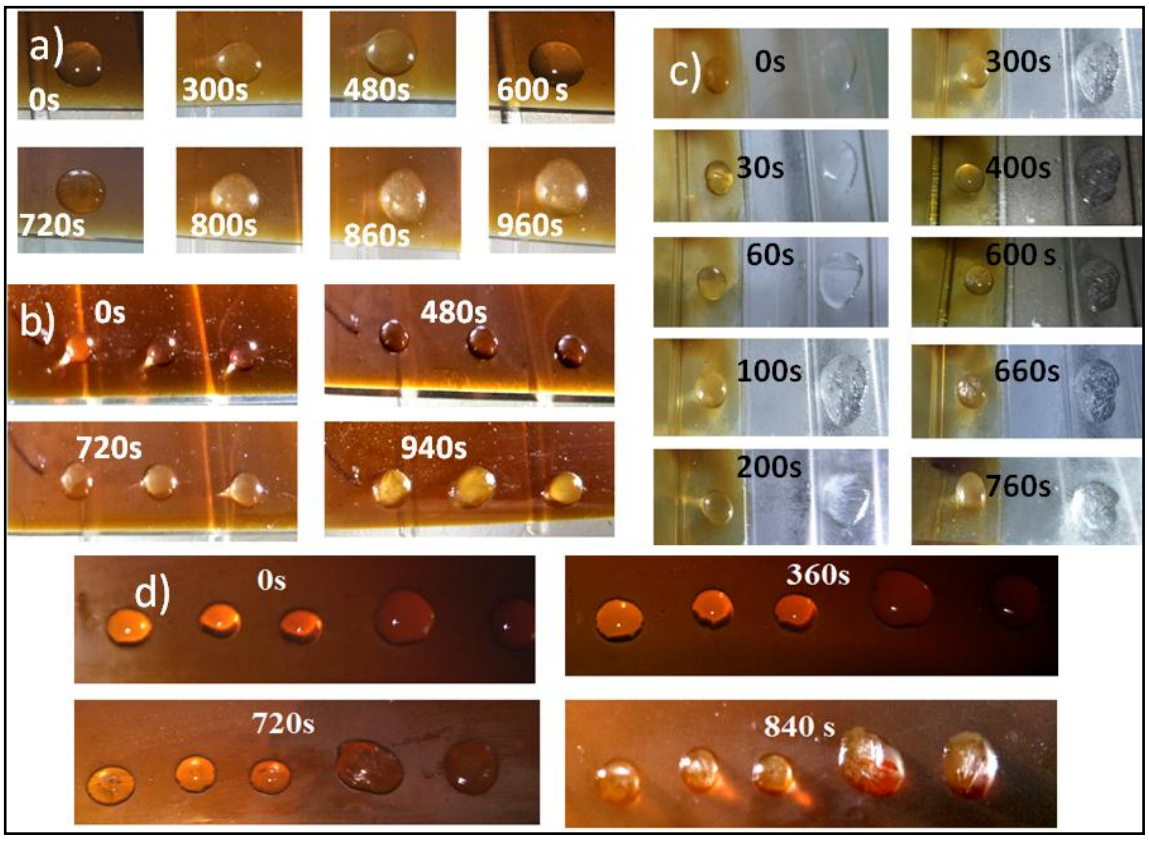

Figure 6B.14: Droplets freezing and icing-delay time for the surfaces of three nanocomposites: **(a, b)** PCTN2.5**, (c)** PCTN0.5 and **(d)** PCTN1 at -15 °C

Ice-phobicity usually refers as an ability to delay or prevent ice nucleation and deposition on surfaces. This can be achieved using surface with high water contact angle and low surface energy. The formation of ice can be prevented via two approaches: one is by reduction of the contact time to help quick shedding of water droplets before ice can nucleate on the surface and other is by delaying heterogeneous nucleation through a combination of surface and therefore being able to prevent the fog formation. The ice formation could delay in superhydrophobic surface owing to the tardy heat conduction as well as high free energy barrier of nucleation. The delayed freezing of water droplets on the superhydrophobic surfaces is explained as follows: rougher the surface is, lower will be the water-solid contact area and hence more entrapped air will be there in the water-solid interface. Therefore, the process of heat exchange between the water droplets and solid slows down because the entrapped air present in water-

surface interface acting as an insulator. This process leads to longer and delayed freezing time of water droplets. Thus, water droplets on coated superhydrophobic surface were frozen with a much longer delay time compared to the uncoated one [66, 69-71].

6B.3.10. Self-cleaning property

The self-cleaning ability of the nanocomposite was evaluated by monitoring the photocatalytic degradation of mixed dye (MB and MO), BPA, phenol, and paraoxon ethyl pesticide under normal sunlight. The UV-vis spectra of these organic contaminants with respect to time on exposure of sunlight are shown in **Figure 6B.15a-g**. The spectrum ranges from 250 to 800 nm with a characteristic absorption peak at wavelength of 466 nm, was observed for methyl orange and 630 nm for MB (**Figure 6B.15a**). It was observed that the peak intensity of both MO and MB decreases with increasing exposure time. However, after 60 min of sunlight exposure the intensity of UV absorption peak of MO was observed to decrease sharply, while intensity of UV absorption peak of MB still remains significantly high. However, after 2 h of sunlight exposure, a rapid rate of degradation for MB was observed. Overall, a higher rate of degradation was observed for MO compared to MB in the mixed dye mixture. This difference implied that the nanocomposite exhibited a superior photocatalytic degradation of MO to MB in the mixed dye system. Lower degradation percentage of MB in the mixture is mainly related with the occurrence of the oxidizing species as well as that the presence of N=N makes MO more reactive, while the presence of -CH_3 groups in MB makes it resistance to photodegradation. However, the overall degradation is due to the fact that the nanocomposites possess large numbers of -COOH and -OH groups which enhances the compatibility with the cationic dyes as well as other organic pollutants. This fact helps in degradation of above contaminants within a short period of time [53]. The degradation efficiency of PCTN2.5 for MO and MB was found to be 99% and 86 % respectively. Further, the degradation efficiency of phenol, BPA and pesticide by PCTN2.5 was found to be 95%, 89% and 91% respectively within 4-4.5 h. These degradation efficiencies were found to be higher than the literature reported values by TiO_2-Pt/Ti (87%) and TiO_2-Ti (55.6%) for BPA [54], and by ZnO@SiO_2 (84%) [55] for phenol under UV light. Further, the rate of degradation was found to increase with the increase in the loading of the nanohybrid (**Figure 6B.15**). This is due to reason that the increase in the number of CD@TiO_2 increases the number of photons absorbed and consequently the number of

the contaminant molecules adsorbed. The enhanced photocatalytic degradation of the nanocomposite is because of the presence of CD. It is well established that CD absorb visible light and then covert them to shorter wavelength which again excites TiO_2 to generate e^-/h^+ pairs. Further, it was also reported that CD of CD@TiO_2 reduces the high recombination rate of e^-/h^+ pairs. Therefore, the combination of CD with TiO_2 would help to prevent the charge recombination and expand the range of light wavelengths adsorbed [32]. A probable mechanism for the degradation organic contaminants is shown in **Scheme 6B.3**. Literature cited that the degradation of organic contaminants is a pseudo first-order reaction and fitted to simplify Langmuir-Hinshelwood model. This model is widely used to investigate photocatalytic process [4, 53, 56]. The degradation kinetics are presented by plotting C_t/C_0 and $\ln(C_0/C_t)$ *vs* time (**Figure 6B.16a-e**). The fitting plots were found to be straight lines for all the nanocomposites, indicating that the degradation of mixed dye as well as other organic contaminants followed first order kinetic. The results were found to be nearly consistent with the linear equation $\ln C_0/C_t = k_t$, where C_0 is the initial concentration of an organic contaminant and C_t is the concentration at time t, and k is the rate constant of the first order reaction. The degradation rate of MO and MB over the nanocomposite was found to be 0.25×10^{-1} min^{-1} and 0.13×10^{-1} min^{-1} respectively, indicating that the degradation of MO was faster than that of MB. These values are found to be superior than literature reported $LiMg_{0.5}Mn_{0.5}O_2$ (0.91×10^{-2} and 0.2×10^{-2} min^{-1} for MO and MB) and TiO_2 powder (0.78×10^{-2} and 0.35×10^{-2} min^{-1} for MO and MB) [56].

Further, the recycling ability of these nanocomposites was checked by degrading the dye mixture repeatedly using the same nanocomposite sample (**Figure 6B.17a, 6B.17b**). The results authenticated no significant decrease in photocatalytic activity of the films. The catalytic activities of the nanocomposite is described from the fact that charge transfer from the excited dye to the catalyst occurs under exposure of sunlight, which consequently helps in self-degradation by oxidizing them. Furthermore, the e^- and h^+ generated upon exposure of sunlight promote the generation of radicals, which can act as strong oxidants contributing to the degradation of the dye. Further, the degradation rate constants (k) for phenol, BPA and pesticide by PCTN2.5 were found to be 0.12×10^{-1}, 0.8×10^{-2} and 0.8×10^{-2} min^{-1} respectively. The rate constant for BPA was found to be higher than reported bare TiO_2 (0.4×10^{-2} min^{-1}), TiO_2/Ti (0.3×10^{-2} min^{-1}) and comparable to RGO/TiO_2 (1.32×10^{-2} min^{-1}) under UV light [57]. The rate constant of

phenol was superior to Ti (0.6×10^{-2} min^{-1}) and RGO/Ti (0.7×10^{-2} min^{-1}) where degradation was performed under UV light [60].

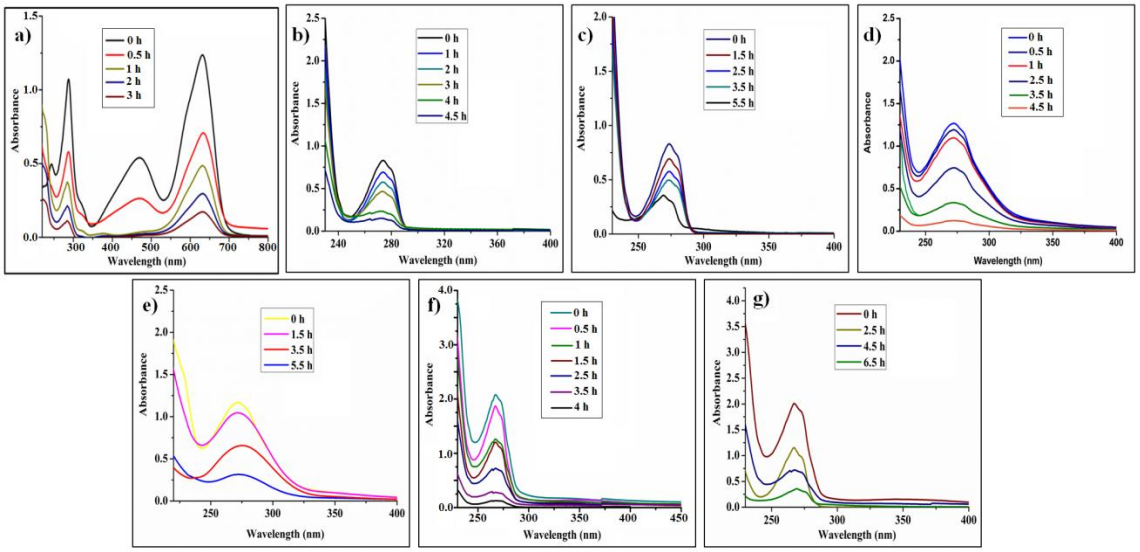

Figure 6B.15: Self-cleaning behavior of the nanocomposites. UV-vis absorption spectra of **(a)** mixed dye in presence of PCTN2.5, **(b, c)** BPA **(d, e)** pesticide and **(f, g)** phenol in presence PCTN2.5 and PCTN0.5 respectively under sunlight irradiation

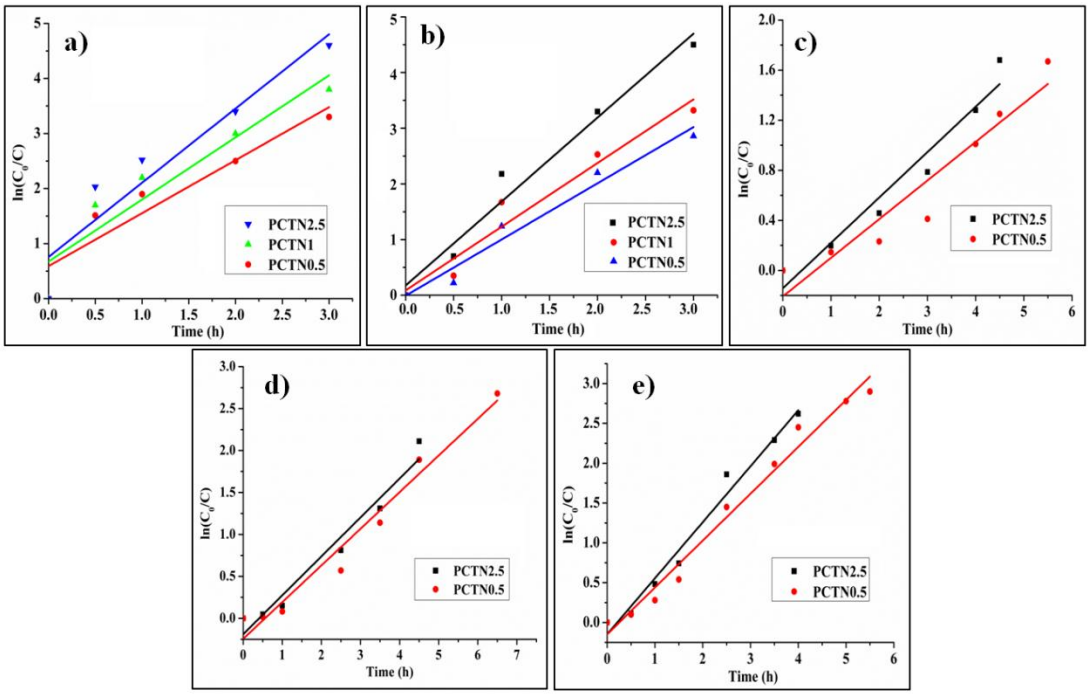

Figure 6B.16: Degradation kinetics of **(a, b)** MB and MO, **(c)** BPA, **(d)** pesticide and **(e)** phenol

Most importantly, to examine the self-cleaning property of the nanocomposite a coating of it was made on the surface of a stone to check the decolorization of methylene blue color under sunlight.

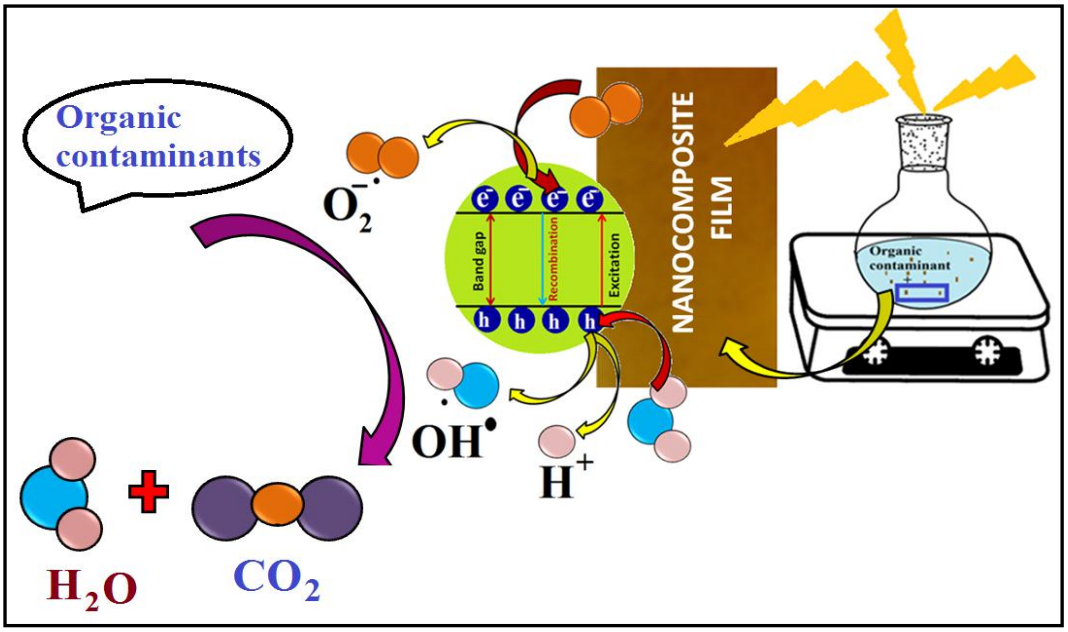

Scheme 6B.3: Mechanism for photocatalytic degradation of organic contaminants by the nanocomposite under sunlight

It was tested simply by carrying out a photodegradation test of MB deposited on the coated and uncoated surfaces of a stone. The change in color of the dye with exposure time was recorded by taking images at different times as shown in **Figure 6B.17c**. The decolorization of the model dirt was observed on the surface of coated stone, whereas the bare stone unable to remove the color of MB. Thus, it can be utilized as a thin film for self-cleaning surfaces and also used for protection of stone-based monuments.

Furthermore, the removal of dye (bromophenol blue) from the nanocomposite surface by water droplet is documented in **Figure 6B.17d** and self-cleaning property was observed. It was observed that the dirt particles were wetted by the water droplet within 45s and imbibed into the droplet as they rolls off on the surface and thereby making the surface clean. This is due to super-hydrophobic nature of the film which is one of the most essential criteria for achieving self-cleaning property [32].

6B.3.11. Photocatalytic activity of the nanocomposite for reduction of 4-NP

The nanocomposite (PCTN2.5) was used as a photocatalyst for obtaining 4-aminophenol from 4-NP under normal sunlight. The reduction process was monitored by taking UV-

vis absorbance spectra at different intervals of time (**Figure 6B.18a**). The color of aqueous solution of 4-NP is yellow and showed an absorption peak at 318 nm in the UV-vis spectrum [72].

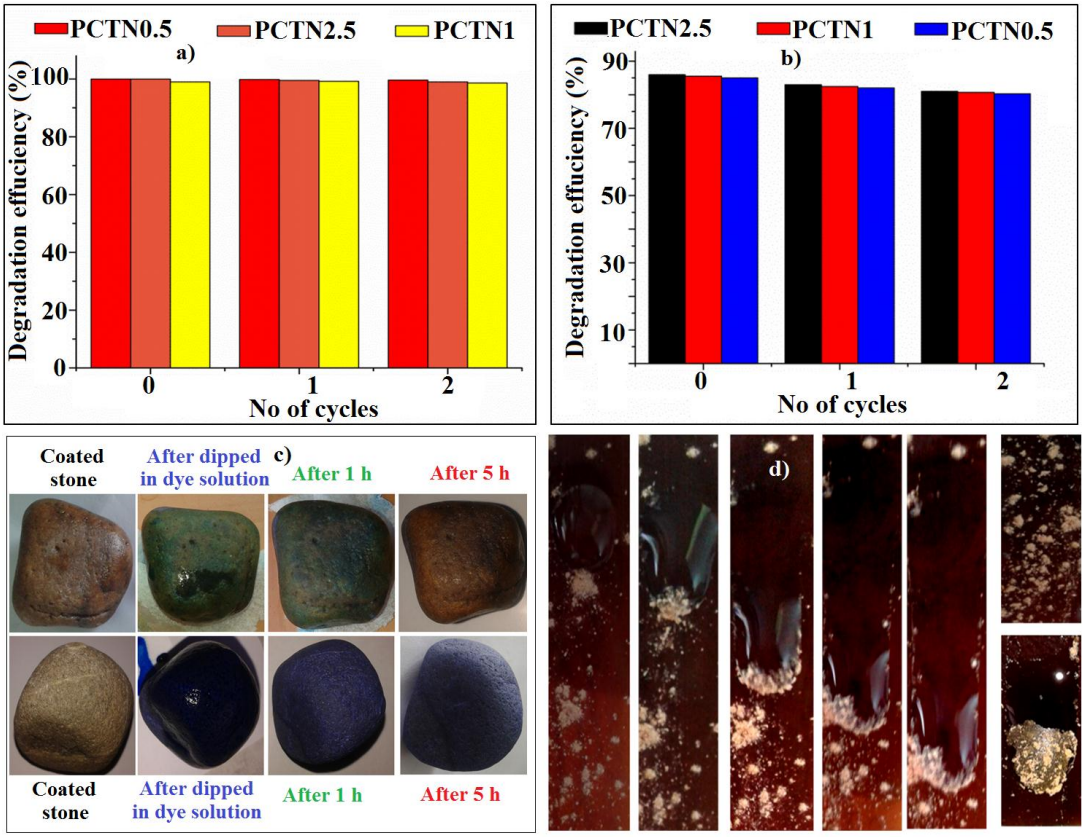

Figure 6B.17: (a, b) Photocatalytic efficiency for degradation of MO and MB, **(c)** color changes at different time intervals of sunlight exposure of coated and uncoated stones and **(d)** images of removal of dye powder by water droplet with time

The color of this solution was changed from light yellow to bright yellow after addition of $NaBH_4$. This is owing to the deprotonation of 4-NP that shifted the peak from 318 nm to 400 nm [73, 74]. When the catalyst was added, the absorption peak at 400 nm gradually decreased (**Figure 6B.18a**), which indicated the progress of reduction reaction of 4-NP. Meanwhile, an absorption characteristic peak at 300 nm was appeared due to the generation of 4-aminophenol. However, no obvious change of the UV-vis absorption spectra was observed over the time of reaction in the absence of the catalyst, confirming that the reduction reaction did not proceed without the catalyst. This catalytic reaction was well studied and reported in literature as a first-order reaction [72-74]. The plot of ln (A_t /A_0) (A_0 is absorbance at t=0 and A_t is absorbance at time t) *vs* reaction time is shown

in **Figure 6B.18b**. A linear correlation between $\ln(A_t/A_0)$ and time was observed for the nanocomposite, indicating that the reaction is a pseudo first order. This linear relationship of the reduction reaction matched well with the first order kinetics, and the rate constant k was found to be 0.02 min^{-1} as determined from the slope of this curve. This value is higher than the Au nanoparticles (0.9×10^{-1} min^{-1}), and Au/Cu nanohybrid (0.13×10^{-1} min^{-1}) based reduction of 4-NP [75]. Furthermore, the color change of the nitrophenol solution was observed immediately on addition of the sufficient amount of the catalyst and the reduction was confirmed by taking the absorbance of the solution before and after addition of the catalyst (**Figure 6B.18c** and **6B.18d**). The rate constant obtained for this condition was found to be 0.86 min^{-1}. The recovery, reusability, stability, and leaching of the catalyst are also important factors for practical applications which can be achieved for this catalyst.

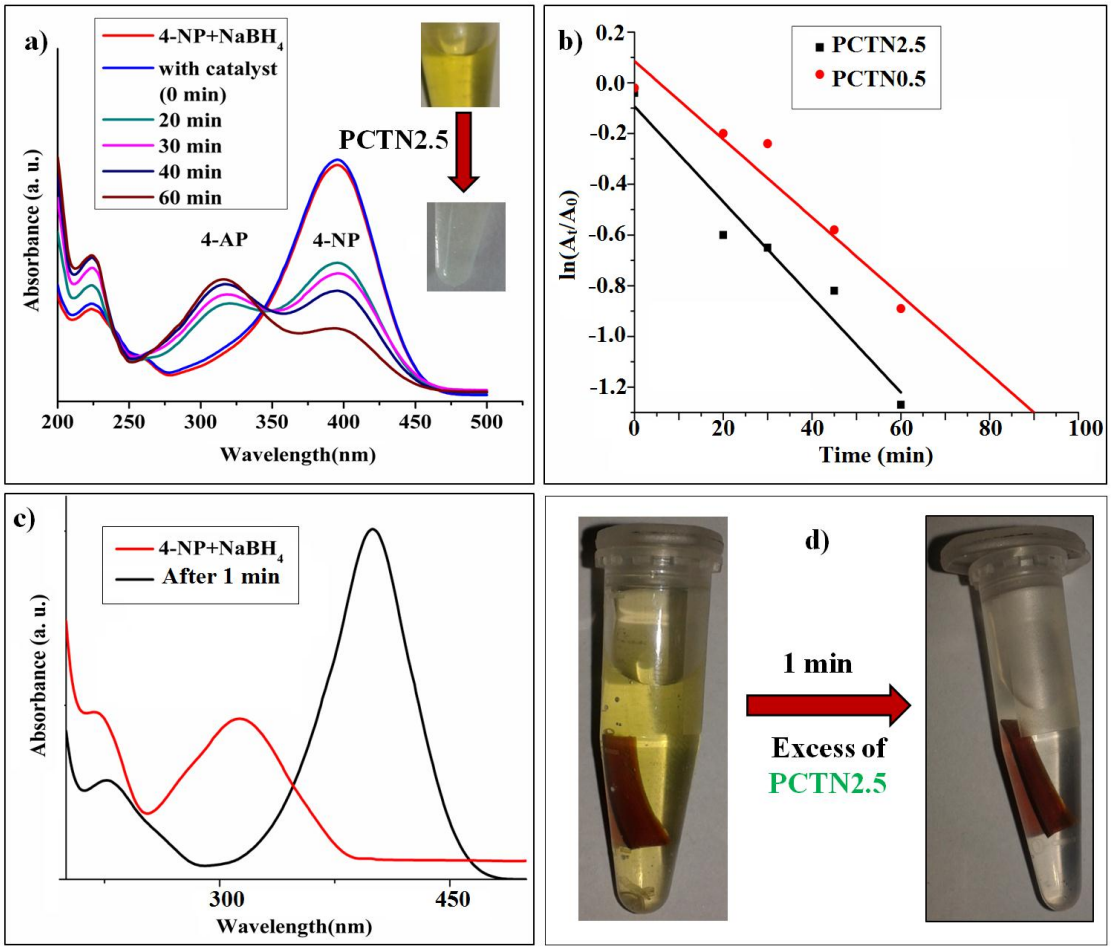

Figure 6B.18: Reduction activity of the nanocomposite. **(a)** UV-vis spectra of 4-NP with time, (**b** plots of ln A_t/A_0 *vs* time and **(c, d)** UV-vis spectra and images of 4-NP after 1 min with excess amount of PCTN2.5

6B.3.12. Antibacterial activity

The antibacterial activity of the nanocomposites was tested against *S. aureus*, *B. subtilis*, *K. pneumoniae* and *P. aeruginosa* bacterial strains by the agar well diffusion method. The bacterial growth curves and the zones of inhibition for the nanocomposite against gram-positive and gram-negative bacteria are shown in **Figure 6B.19**. From the curves (**Figure 6B.19a and b**), it is found that the bacterial growths for all the tested bacteria were completely inhibited by the nanocomposites at all dose levels of the nanohybrid. It was also seen that the nanocomposites formed clear inhibition zones against the tested microbes and the diameter of the inhibition zone increases with increase in the amount of the nanohybrid (**Figure 6B.19c-f**). Thus, all the nanocomposites exhibited significant antibacterial activity towards different gram positive and gram negative bacteria. The maximum zone of inhibition in the nanocomposites was observed against *B. subtilis* and *P. aeruginosa*.

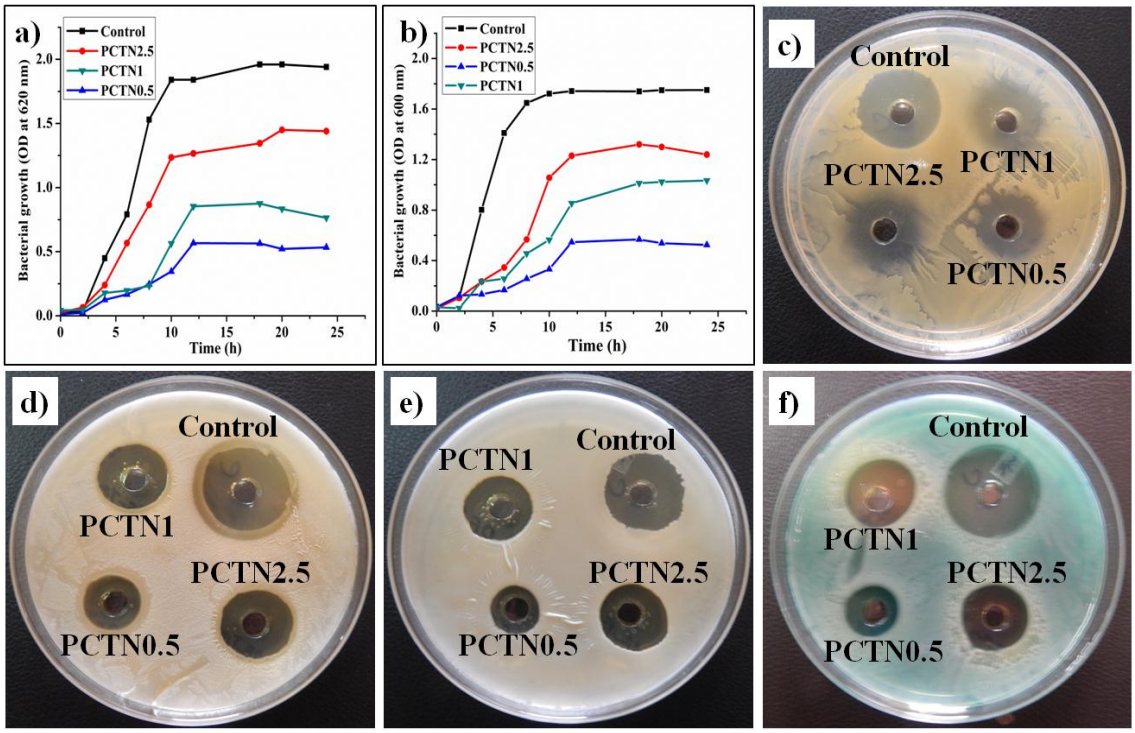

Figure 6B.19: Bacterial growth of the nanocomposites against **(a)** *P. aeruginosa* and **(b)** *S. aureus* and the zone of inhibition test results of the nanocomposite against **(c)** *S. aureus*, **(d)** *K. pneumoniae*, **(e)** *B. subtilis* and **(f)** *P. aeruginosa*

The results indicate ability of the nanohybrid to provide bacterial contaminant free nanocomposite films. The main mechanism of antibacterial activity is because of the

oxidative stress induced by production of reactive oxygen species by TiO_2. In literature, there are many reports which explored the photogeneration of reactive oxygen species on the surfaces of metal-oxide nanoparticles [42, 43]. The common principle is that upon exposure of light with photoenergy larger than the band gap, the electrons of TiO_2 are promoted across the band gap to the conduction band and creates a hole in the valence band. However, in case of nanocomposite, CD absorbs visible light during the test and emits shorter wavelength of light which again excites TiO_2 nanoparticles to form e^-/h^+ pairs, which reacts with O_2 through a reductive process and H_2O through a oxidative process to produce active oxygen radicals like $^{\bullet}O_2^-$ and $^{\bullet}OH$. Singlet oxygen ($^1O_2$) is indirectly formed from aqueous reactions of $O_2^{\bullet-}$. The holes, superoxide ion and $^{\bullet}OH$ are very potent oxidants which used to naturally decompose and oxidize common organic substance such as odor molecules, bacteria and viruses to water and carbon dioxide. Among them, $^{\bullet}OH$ is a nonselective and strong oxidant and plays the most significant role in inactivating the microorganism. Although $O_2^{\bullet}$ is not a powerful oxidant, but showed considerable biological implications as a precursor for $^1O_2$ and $^{\bullet}OH$. Therefore, these three types of reactive oxygen species ($^{\bullet}OH$, $O_2^{\bullet}$ and $^1O_2$) took part to the main oxidative stress in the biological systems [42, 43].

6B.3.13. Separation oil and water from their mixture

The separation of oil and water from their mixture is a daunting challenge because of the increasing industrial oil contaminated water as well as the frequent oil spill accidents occurring across the globe. Thus, the nanocomposite with excellent mechanical properties and repellency to crude oil showed potential to further develop as an advanced oil/water separation membrane. The separation of oil and water from its mixture was performed as shown in **Figure 6B.20 (a-d)**. The figure clearly revealed the efficient separation of the components using the nanocomposite membrane, while no separation was observed under normal filtering system. The permeability flux of the nanocomposite membrane was calculated using **Eq. 6B.3** by recording time taken for collection of measured volume of water from its oil-water mixture and the value was found to be 660 $mLm^2\ h^{-1}$. Further, the separation efficiency or oil rejection coefficient was calculated according to **Eq. 6B.1** and it was found to be 99% (5 min). This efficiency (99%) was found to be same as calculated using **Eq. 6B.2** from UV-vis spectral analysis (**Figure 6B.20e**). The value is higher than cellulose nanofiber aerogel (98.6%) [76], and comparable to chitosan based aerogel membrane (99%) [77]. Furthermore, the

microscopic images of feed and the filtrate are shown in **Figure 6B.20f** and **6B.20g**, which confirmed the complete separation. Most importantly, the recyclability of the nanocomposite membrane was examined for oil-water separation upto 4th cycle without any loss of separation efficiency (**Figure 6B.20h**). Thus, the nanocomposite based membrane possesses high potential to be used for separation of industrially oil-polluted water.

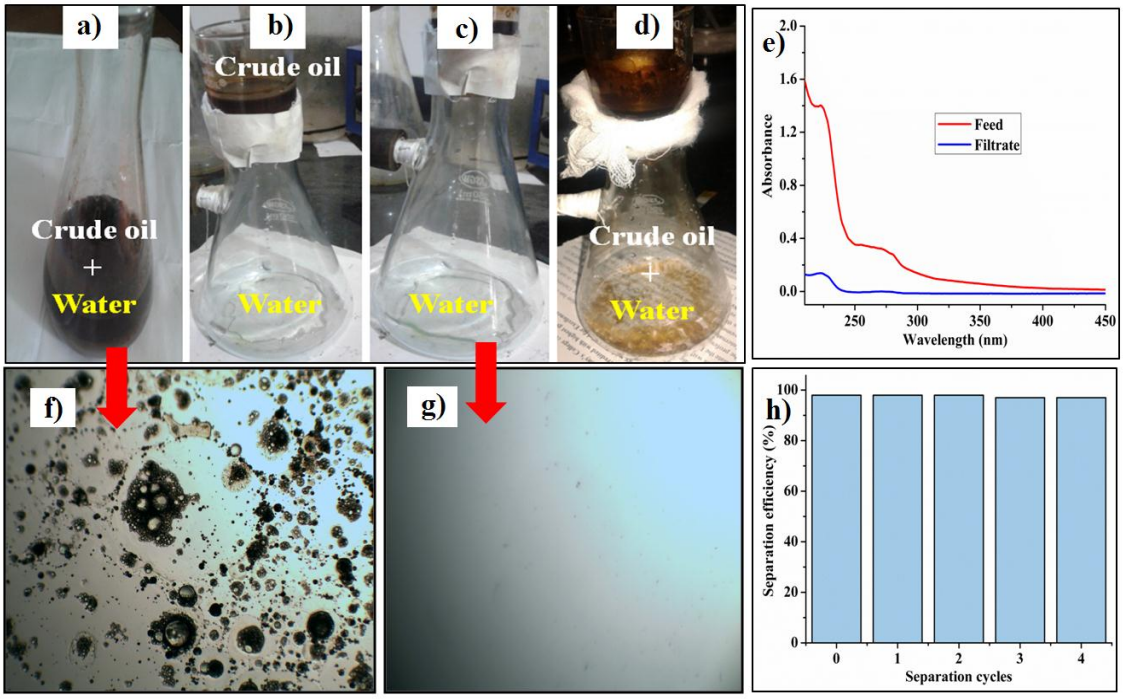

Figure 6B.20: Separation of crude oil and water from their mixture by the nanocomposite**.** Images of **(a)** crude oil and water mixture, **(b-d)** separation of the components at different times by coated (**b** and **c**) and uncoated filter papers **(d**), **(e)** UV-vis spectra, **(f, g)** microscopic images of feed and the filtrate and **(h)** separation efficiency of the nanocomposite membrane

6B.4. Conclusion

Thus, the multi-functional WHPE/CD@TiO_2 nanocomposite was fabricated for the first time through a greener *in-situ* method without using solvent and catalyst. The nanocomposite exhibited excellent mechanical and thermal properties along with wavelength dependent both down- and up-conversion PL properties. Most interestingly, the multi-faceted attributes like anti-reflecting, anti-icing, anti-fogging and self-cleaning properties were observed in the same nanocomposite which is rare to achieve. The

nanocomposite not only able to degrade different organic contaminants but it can also be recycled. In addition, this nanocomposite has the ability to be used as a preservative material for graffiti and as anti-counterfeiting material. This novel material can also be used as an efficient photocatalyst for the reduction of nitrophenol to aminophenol under exposure of sunlight. It can also able to separate crude oil from water efficiently and this study also provides a facile and fast approach for the removal of oil from water. Therefore, this multi-functional nanocomposite has great potential for multi-faceted advanced applications.

References

[1] Li, H., Liu, R., Liu, Y., Huang, H., Yu, H., Ming, H., Lian, S., Lee, S. T., and Kang, Z. Carbon quantum dots/Cu_2O composites with protruding nanostructures and their highly efficient (near) infrared photocatalytic behaviour. *Journal of Materials Chemistry*, 22(34):17470-17475, 2012.

[2] Yeung, K. L. A., Maira, J., Stolz, J., Hung, E., Ho, N. K. C., Wei, A. C., Soria, J., Chao, K. J., and Yue, P. L. Ensemble effects in nanostructured TiO_2 used in the gas-phase photooxidation of trichloroethylene. *Journal of Physical Chemistry B*, 106(18):4608-4616, 2002.

[3] Ming, H., Ma, Z., Liu, Y., Pan, K., Yu, H., Wang, F., and Kang, Z. Large scale electrochemical synthesis of high quality carbon nanodots and their photocatalytic property. *Dalton Transactions*, 41(31):9526-9531, 2012.

[4] Gupta, V. K., Jain, R., Mittal, A., Saleh, T. A., Nayak, A., Agarwal, S., and Sikarwar, S. Photocatalytic degradation of toxic dye amaranth on TiO_2/UV in aqueous suspensions. *Materials Science and Engineering: C*, 32(1):12-17, 2012.

[5] Xu, Y. J., Zhuang, Y., and Fu, X. New insight for enhanced photocatalytic activity of TiO_2 by doping carbon nanotubes: A case study on degradation of benzene and methyl orange. *Journal of Physical Chemistry C*, 114(6):2669-2676, 2010.

[6] Bian, J., Huang, C., Wang, L., Hung, T., Daoud, W. A., and Zhang, R. Carbon dot loading and TiO_2 nanorod length dependence of photoelectrochemical properties in carbon dot/TiO_2 nanorod array nanocomposites. *ACS Applied Materials & Interfaces*, 6(7):4883-4890, 2014.

[7] Yu, X., Liu, J., Yu, Y., Zuo, S., and Li, B. Preparation and visible light photocatalytic activity of carbon quantum dots/TiO_2 nanosheet composites. *Carbon*, 68:718-724, 2014.

[8] Zhang, Y. Q., Ma, D. K., Zhang, Y. G., Chen, W. and Huang, S. M. N-doped carbon quantum dots for TiO_2-based photocatalysis and dye-sensitized solar cells. *Nano Energy*, 2(5):545-552, 2013.

[9] Li, H., He, X., Kang, Z., Huang, H., Liu, Y., Liu, J., Lian, S., Tsang, C. H. A., Yang, X., and Lee, S. T. Water-soluble fluorescent carbon quantum dots and photocatalyst design. *Angewandte Chemie*, 49(26):4430-4434, 2010.

[10] Zhang, H., Ming, H., Lian, S., Huang, H., Li, H., Zhang, L., Liu, Y., Kang, Z., and Lee, S. T. Fe_2O_3/carbon quantum dots complex photocatalysts and their enhanced photocatalytic activity under visible light. *Dalton Transactions*, 40(41):10822-10825, 2011.

[11] Yu, H., Zhang, H., Huang, H., Liu, Y., Li, H., Ming, H., and Kang, Z. ZnO/carbon quantum dots nanocomposites: One-step fabrication and superior photocatalytic ability for toxic gas degradation under visible light at room temperature. *New Journal of Chemistry*, 36(4):1031-1035, 2012.

[12] Dey, D., Bhattacharya, T., Majumdar, B., Mandani, S., Sharma, B., and Sarma, T. K. Carbon dot reduced palladium nanoparticles as active catalysts for carbon-carbon bond formation. *Dalton Transanctions*, 42(38):13821-13825, 2013.

[13] Yin, B., Deng, J., Peng, X., Long, Q., Zhao, J., Lu, Q., Chen, Q., Li, H., Tang, H., Zhang, Y., and Yao, S. Green synthesis of carbon dots with down- and up-conversion fluorescent properties for sensitive detection of hypochlorite with a dual-readout assay. *Analyst*, 138(21):6551-6557, 2013.

[14] De, K., Gupta, K., Mandal, M., and Karak, N. Biocide immobilized OMMT-carbon dot reduced Cu_2O nanohybrid/hyperbranched epoxy nanocomposites: Mechanical, thermal, antimicrobial and optical properties. *Materials Science and Engineering: C*, 56:74-83, 2015.

[15] Pan, J., Sheng, Y., Zhang, J., Wei, J., Huang, P., Zhang, X., and Feng, B. Preparation of carbon quantum dot/TiO_2 nanotubes composites and their visible light catalytic applications. *Journal of Materials Chemistry A*, 2(10):3344-3351, 2014.

[16] Bineesh, K. V., Kim, D. K., and Park, D. W. Synthesis and characterization of zirconium-doped mesoporous nano-crystalline TiO_2. *Nanoscale*, 2(7):1222-1228, 2010.

[17] Jafry, H. R., Liga, M. V., Li, Q., and Barron, A. R. Simple route to enhanced photocatalytic activity of P25 titanium dioxide nanoparticles by silica addition. *Environmental Science & Technology*, 45(4):1563-1568, 2011.

[18] De, B., Voit, B., and Karak, N. Carbon dot reduced Cu_2O nanohybrid/hyperbranched epoxy nanocomposite: Mechanical, thermal and photocatalytic activity. *RSC Advances*, 4(102): 58453-58459, 2014.

[19] Lin, Y., Li, D., Hu, J., Xiao, G., Wang, J., Li, W., and Fu, X. Highly efficient photocatalytic degradation of organic pollutants by PANI-modified TiO_2 composite. *Journal of Physical Chemistry C*, 116(9):5764-5772.

[20] Wang, W., Serp, P., Kalck, P., and Faria, J. L. Photocatalytic degradation of phenol on MWNT and titania composite catalysts prepared by a modified sol-gel method. *Applied Catalysis B: Environmental*, 56:305-312, 2005.

[21] Zhu, S., Song, Y., Zhao, X., Shao, J., Zhang, J., and Yang, B. The photoluminescence mechanism in carbon dots (graphene quantum dots, carbon nanodots, and polymerdots): Current state and future perspective. *Nano Research*, 8(2):355-381, 2015.

[22] Wang, P., Zhai, Y., Wang, D., and Dong, S. Synthesis of reduced graphene oxide-anatase TiO_2 nanocomposite and its improved photo-induced charge transfer properties. *Nanoscale*, 3(4):1640-1645, 2011.

[23] De, B. and Karak, N. A green and facile approach for the synthesis of water soluble fluorescent carbon dots from banana juice. *RSC Advances*, 3(22):8286-8290, 2013.

[24] Zhang, H., Zhao, L., Geng, F., Guo, L. H., Wan, B., and Yang, Y. Carbon dots decorated graphitic carbon nitride as an efficient metal-free photocatalyst for phenol degradation. *Applied Catalysis. B: Environmental*, 180:656-662, 2016.

[25] Alam, A. M., Park, B. Y., Ghouri, Z. K., Parkc, M., and Kim, H. Y. Synthesis of carbon quantum dots from cabbage with down- and up-conversion fluorescence properties: excellent imaging agent for biomedical applications. *Green Chemistry*, 17(7):3791-3797, 2015.

[26] Ma, Z., Ming, H., Huang, H., Liu, Y., and Kang, Z. One-step ultrasonic synthesis of fluorescent N-doped carbon dots from glucose and their visible-light sensitive photocatalytic ability. *New Journal of Chemistry*, 36(4):861-864, 2012.

[27] Tu, K., Wang, Q., Lu, A., and Zhang, L. Portable visible-light photocatalysts constructed from Cu_2O nanoparticles and graphene oxide in cellulose matrix. *Journal of Physical Chemistry C*, 118(13):7202-7210, 2014.

[28] Khezrianjoo, S. and Revanasiddappa, H. D. Langmuir-Hinshelwood kinetic expression for the photocatalytic degradation of metanil yellow aqueous solutions by ZnO catalyst. *Chemical Sciences Journal*, 85:1-7, 2012.

[29] Ku, Y. and Jung, I. L. Photocatalytic reduction of Cr(VI) in aqueous solutions by UV irradiation with the presence of titanium dioxide. *Water Research*, 35(1):135-142, 2001.

[30] Gayaa, U. I. and Abdullaha, A. H. Heterogeneous photocatalytic degradation of organic contaminants over titanium dioxide: A review of fundamentals, progress and problems. *Journal of Photochemiscry and Photobiology C: Photochemistry Reviews*, 9(1):1-12, 2008.

[31] Kumar, K., Ghosh, P. K., and Kumar, A. Improving mechanical and thermal properties of TiO_2 nanocomposites. *Composites Part B*: *Engineering*, 97:353-360, 2016.

[32] Charpentier, P. A., Burgess, K., Wang, L., Chowdhury, R. R., Lotus, A. F., and Moula, G. TiO_2/polyurethane composites for antibacterial and self-cleaning coatings. *Nanotechnology*, 23(42):425-606, 2012.

[33] Santos, L. M., Carone, C. L. P., Einloft, S. M. O., and Ligabue, R. A. Preparation and properties of aromatic polyester/TiO_2 nanocomposites from polyethylene terepthalate. *Materials Research*, 19(1):158-166, 2016.

[34] Ghanem, A. F., Badawy, A. A., Ismailb, N., Tian, Z. R., Rehim, M. H. A., and Rabia, A. Photocatalytic activity of hyperbranched polyester/TiO_2 nanocomposites. *Applied Catalysis A: General*, 472:191-197, 2014.

[35] Rahman, O. and Ahmad, S. Soy polyester urethane/TiO_2 and Ce-TiO_2 nanocomposites: Preparation, characterization and evaluation of electrochemical corrosion resistance performances. *RSC Advances*, 6(13):10584-10596, 2016.

[36] Ingole, P. G., Baig, M. I., Choi, W. K., and Lee, H. K. Synthesis and characterization of polyamide/polyester thin-film nanocomposite membranes achieved by functionalized TiO_2 nanoparticles for water vapour separation. *Journal of Materials Chemistry A*, 4(15):5592-5604, 2016.

[37] Khaled, S. M., Sui, R., Charpentier P. A., and Rizkalla, A. S. Synthesis of TiO_2-PMMA nanocomposite: Using methacrylic acid as a coupling agent. *Langmuir*, 23(7):3988-3995, 2007.

[38] Paul, D. R. and Robeson, L. M. Polymer nanotechnology: Nanocomposites. *Polymer*, 49(15):3187-3204, 2008.

[39] Lu, X., Wang, Z., Yang, X., Xu, X., Zhang, L., Zhao, N., and Xu, J. Antifogging and antireflective silica film and its application on solar modules. *Surface and Coatings Technology*, 206(6):1490-1494, 2011.

[40] England, M. W., Urata, C., Dunderdale, G. J., and Hozum, A. Anti-fogging/self-healing properties of clay-containing transparent nanocomposite thin films. *ACS Applied Materials & Interfaces*, 8(7):4318-4322, 2016.

[41] Hu, X., Yu, Y., Wang, Y., Zhou, J., and Song, L. Highly transparent superhydrophilic graphene oxide coatings for anti-fogging. *Materials Letters*, 182:372-375, 2016.

[42] Fernando, K. A. S., Sahu, S., Liu, Y., Lewis, W. K., Guliants, E. A., Jafariyan, A., Wang, P., Bunker, C. E., and Sun, Y. P. Carbon quantum dots and applications in photocatalytic energy conversion. *ACS Applied Materials & Interfaces*, 7(16):8363-8376, 2015.

[43] Zhou, L., He, B., and Huang, J. Amphibious fluorescent carbon dots: One-step green synthesis and application for light-emitting polymer nanocomposites. *Chemical Communications*, 49(73):8078-8080, 2013.

[44] Zhang, G., Ke, Y., Song, Y., Lu S., and Wang, Z. Preparing copolyester–titanium dioxide nanocomposites with low melting point via in situ hydrolysis, catalysis and esterification process. *High Performing Polymers*, 28(4):445-452, 2015.

[45] Dai, J., Ma, S., Wu, Y. Han, L., Zhang, L., Zhu, J., and Liu. X. Polyesters derived from itaconic acid for the properties and bio-based content enhancement of soybean oil-based thermosets. *Green Chemistry*, 17(4): 4291-4299, 2015.

[46] Zhao, Y., Wang, F., Fu, Q., and Shi, W. Synthesis and characterization of ZnS/hyperbranched polyester nanocomposite and its optical properties. *Polymer*, 48(10):2853-2859, 2007.

[47] Hazarika, D. and Karak, N. Photocatalytic degradation of organic contaminants under solar light using carbon dot/titanium dioxide nanohybrid obtained through a facile approach. *Applied Surface Science*, 376:276-285, 2016.

[48] Yang, J., Huo, J., Chen, F., Yang, Q., and Hou, X. Oil/water separation based on natural materials with super wettability: Recent advances. *Physical Chemistry Chemical Physics*, 20(39):25140-25163, 2018.

[49] Wu, Z., Li, Y., Zhang, L., Zhong, Y., Xu, H., Mao, Z., Wang, B., and Sui, X. Thio-ene click reaction on cellulose sponge and its application for oil/water separation. *RSC Advances*, 7(33):20147-20151, 2017.

[50] Chen, J., Zhou, Y., Nan, Q., Sun, Y., Ye, X., and Wang, Z. Synthesis, characterization and infrared emissivity study of polyurethane/TiO_2 nanocomposites. *Applied Surface Science*, 2007, 253(23):9154-9158, 2017.

[51] Benavides, E. E. U., Kayatin, M. J., and Davis, V. A. Dispersion and rheology of multiwalled carbon nanotubes in unsaturated polyester resin. *Macromolecules*, 46(4):1642-1650, 2013.

[52] Tang, Y., Hu, X., Zhang, X., Guo, D., Zhang, J., and Kong, F. Chitosan/titanium dioxide nanocomposite coatings: Rheological behavior and surface application to cellulosic paper. *Carbohydrate Polymers*, 15:752-759, 2016.

[53] Yang, J., Han, C. R., Duan, J. F., Xu, F., and Sun, R. C. Mechanical and viscoelastic properties of cellulose nanocrystal reinforced poly(ethylene glycol) nanocomposite hydrogel. *ACS Applied Materials & Interfaces*, 5(8):3199-3207, 2013.

[54] De, B., Voit, B., and Karak, N. Transparent luminescent hyperbranched epoxy/carbon oxide dot nanocomposites with outstanding toughness and ductility. *ACS Applied Materials & Interfaces*, 5(20):10027-10034, 2013.

[55] Beg, M. D. H., Moshiul, A. K. M., Yunus, R. M., and Mina, M. F. Improvement of interaction between pre-dispersed multi-walled carbon nanotubes and unsaturated polyester resin. *Journal of Nanoparticle Research*, 7:2846-2848, 2015.

[56] Salehian, H., Ahmad, S., and Jahromi, J. Effect of titanium dioxide nanoparticles on mechanical properties of vinyl ester-based nanocomposites. *Journal of Composite Materials*, 49:2365-2373, 2015.

[57] Nguyen, V. G., Thai, H., Mai, D. H., Tran, H. T., Tran, D. L., and Vu, T. Effect of titanium dioxide on the properties of polyethylene/TiO_2 nanocomposites. *Composite Part B: Engineering*, 45:1192-1198, 2013.

[58] Dalir, H., Farahani, R. D., Nhim, V., Samson, B., Levesque, M. L., and Therriault, D. Preparation of highly exfoliated polyester-clay nanocomposites: Process-property correlations. *Langmuir*, 28(1):791-803, 2012.

[59] Hazarika, D. and Karak, N. Biodegradable tough waterborne hyperbranched polyester/carbon dot nanocomposite: Approach towards an eco-friendly material. *Green Chemistry*, 18(19):5200-5211, 2016.

[60] Han, K. and Yu, M. Study of the preparation and properties of UV-blocking fabrics of a PET/TiO_2 nanocomposite prepared by in situ polycondensation. *Journal of Applied Polymer Scien*ce, 100(2):1588-1593, 2006.

[61] Silva, V. D., Santos, L. M., Subda, S. M., Ligabue, R., Seferin, M., Carone, C. L. P., and Einloft, S. Synthesis and characterization of polyurethane/titanium dioxide nanocomposites obtained by in situ polymerization. *Polymer Bulletin*, 70(6):1819-1833, 2013.

[62] Chakradhar, K. V. P., Subbaiah, K. V., Kumar, M. A., and Reddy, G. R. Blended epoxy/polyester polymer nanocomposites: Effect of "Nano" on mechanical properties. *Polymer-Plastics Technology and Engineering*, 51(1):92-96, 2012.

[63] Zhang, H., Huang, J., Yang, L., Chen, R., Zou, W., Lin, X. and Qu, J. Preparation, characterization and properties of PLA/TiO_2 nanocomposites based on a novel vane extruder. *RSC Advances*, 5(6):4639-4647, 2015.

[64] Pascual, A. M. and Vicentec, A. L. Effect of TiO_2 nanoparticles on the performance of polyphenylsulfone biomaterial for orthopaedic implants. *Journal of Materials Chemistry*, B, 2(43):7502-7514, 2014.

[65] Tomma, B. J. A. J. H. and Matty, F. S. Synthesis, characterization and study of mechanical properties for blended nanocomposites based on new epoxy resin. *Journal of Natural Sciences Research*, 5(18):2224-3186, 2015.

[66] Polizos, G., Tuncer, E., Sauers, I., and More, K. L. Physical properties of epoxy resin/titanium dioxide nanocomposites. *Polymer Engineering and Science*, 51(1):87-93, 2011.

[67] Anastas, P. and Eghbali, N. Green Chemistry: Principles and practice. *Chemical Society Reviews*, 39(1):301-312, 2010.

[68] Singh, R., Sureshn G., and Shrikant, S. Thermal and mechanical properties of nano-titanium dioxide doped polyvinyl alcohol. *Polymer Bulletin*, 70(4):1251-1264, 2013.

[69] Chen, D., Zou, L., Li, S., and Zheng, F. TiO_2 nanotubes wrapped with reduced graphene oxide as a high-performance anode material for lithium-ion batteries. *Scientific Reports*, 6:1-8, 2016.

[70] Jesus, M. A. M. L., Neto, J. T. S., Timo, G., Paiva, P. R. P., Dantas, M. S. S., and Ferreira, A. M. Superhydrophilic self-cleaning surfaces based on $TiO_2$and TiO_2/SiO_2 composite films for photovoltaic module cover glass. *Applied Adhesion Science*, 3(1):5, 2015.

[71] Hooda, A., Goyat, M. S., Gupta, R., Prateek, M., Agrawal, M., and Biswas, A. Synthesis of nano-texured polystyrene/ZnO coatings with excellent transparency and superhydrophobicity. *Materials Chemistry and Physics*, 193:447-452, 2017.

[72] Chen, H., Chen, S., Quan, X., Yu, H., Zhao, H., and Zhang, Y. Fabrication of TiO_2-Pt coaxial nanotubes array schottky structures for enhanced photocatalytic degradation of phenol in aqueous solution. *Journal of Physical Chemistry C*, 112(25):9285-9290, 2008.

[73] Wongkalasin, P., Chavadej, S., and Sreethawong, T. Photocatalytic degradation of mixed azo dyes in aqueous wastewater using mesoporous-assembled TiO_2 nanocrystal synthesized by a modified sol-gel process.. *Colloids and Surfaces A: Physicochemical and Engineering Aspects*, 384(1-3):519-528, 2011.

[74] Kurod, K., Ishid T., and Harut, M. J. Reduction of 4-nitrophenol to 4-aminophenol over Au nanoparticles deposited on PMMA, *Molecular Catalysis A: Chemical*, 298(1-2):7-11, 2009.

[75] Jansanthea, P., Boonprakob, N., Treenattip, J., Pookmanee, P., and Phanichphant, S. Photocatalytic degradation of methylene blue and methyl orange over TiO_2 powder synthesized via the solvothermal method. *Applied Mechanics and Materials*, 749:51-55, 2015.

[76] He, Z., Zhang, X., and Batchelor, W. Cellulose nanofibre aerogel filter with tuneable pore structure for oil/water separation and recovery. *RSC Advances*, 6(26):21435–21438, 2016.

[77] Chaudhary, J. P., Vadodariya, N., Nataraj, S. K., and Meena, R. Chitosan-based aerogel membrane for robust oil-in-water emulsion separation. *ACS Applied Materials & Interfaces*, 7(44):24957-24962, 2015.